Characterization and optimization of aluminum oxide films as p-type Czochralski silicon passivation layer

Goverde, J.C.

Award date:
2012

Eindhoven University of Technology
Department of Applied Physics
Plasma & Material Processing

Characterization and optimization of Aluminum Oxide films as *p*-type Czochralski silicon passivation layer

J.C. Goverde

Mei 2012 PMP 12-06

Under Supervision of:
Dr. B. Vermang
Dr. J. John

Graduation professor:
Prof. dr. ir. W.M.M. Kessels

Abstract

The effect of a thermal treatment on the material and layer properties of aluminum oxide (Al_2O_3) thin films deposited by atomic layer deposition has been investigated in order to optimize the functionality of Al_2O_3 as surface passivation layer in *p*-type silicon solar cells.

It has been shown that the fixed charge density, surface defect density, silicon oxide interfacial layer, film stress, crystal phase and atomic composition are influenced significantly by a post-deposition treatment. (i) Negative fixed charges and a silicon oxide interfacial layer are formed, (ii) H_2O, H_2 and CO_2 effuse from the Al_2O_3 layer, and (iii) the film stress increases during a thermal anneal in N_2 environment. (iv) Thick (30 nm) amorphous Al_2O_3 layers transform into γ-Al_2O_3 upon annealing at 800 ˚C. Furthermore, blister formation has been observed during thermal treatment. Blisters can be formed due to the increased film stress and the capping effect of the dielectric layer which prevents the diffusion of species, causing delamination of the film.

The passivation quality of rapidly thermally annealed Al_2O_3/a-SiN_x:H stacks has been optimized, so that the stacks function as rear surface passivation stack in *p*-type Czochralski silicon solar cells. The effective minority carrier lifetime in the silicon was measured to determine the passivation quality of the stack. It has been shown that its passivation quality is reduced during the rapid thermal anneal due to (i) blister formation and (ii) an increase of the interface defect density. It has been proven that blister formation should be avoided to achieve the highest level of surface passivation. Blister-free passivation stacks can be manufactured by outgassing Al_2O_3 layers prior to a-SiN_x:H deposition. The highest level of surface passivation is provided by Al_2O_3/a-SiN_x:H stacks with 10 nm thick Al_2O_3 films annealed at 600 ˚C for 20 minutes in N_2 environment.

By integrating the optimized stacks into *p*-type Czochralski Passivated Emitter and Rear Cell (PERC) silicon solar cells, the average open circuit voltage increased by 5.1 mV compared to the open circuit voltage of industrial PERC (*i*-PERC) silicon solar cells. Furthermore, an alternative solar cell production sequence is designed by using blistered passivation stacks.

Table of Contents

1. Introduction and motivation

1.1.Energy market

The importance of renewable energy sources is clearer than ever; the effect of the global warming as a consequence of the greenhouse effect and the limited availability of fossil fuels makes the human society realize that it is time to change its energy concepts.

Nowadays, close to 90 % of the energy used worldwide is produced out of fossil fuels [1]. In order to minimize the ecological footprint, the energy mix should transform from a fossil fuel based towards a renewable based energy mix. Figure 1 depicts the development of the energy consumption and the energy mix over time. Furthermore, Figure 1 shows numerous possible transformation scenarios for 2050 [1]. Each scenario represents an energy mix with different, not specified assumptions. All scenarios are restricted by an anthropogenic heating of maximum 2 ˚C.

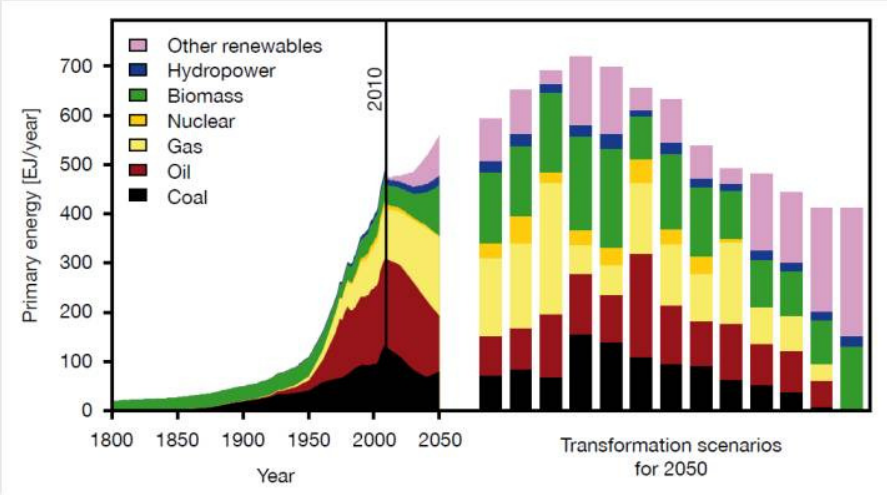

Figure 1: The energy consumption and energy mix over the last few years and transformation scenarios for energy mixes in 2050. The scenarios are restricted by anthropogenic heating of maximum 2 ˚C [1].

As depicted in Figure 1, every scenario shows that a large part of the energy needs to be produced out of renewable energy sources, such as wind, biomass and solar power. The reduction of the greenhouse effect by the use of biomass is doubtful, and not every location is suitable for the production of wind energy. Solar light on the other hand can be converted into electricity on almost every spot on earth, making photovoltaic (PV) devices a good candidate for the production of energy from renewable sources. Figure 2 shows the global interest in the PV market. The total PV capacity shows an exponential growth over years and this trend is expected to last up to 2015 [1].

1.2. Photovoltaic technologies

In 1839 Becquerel observed that certain materials, when exposed to light, produced an electric current [2]. Nowadays, this is known as the photoelectric effect, where electrons are emitted from matter as a consequence of their absorption of a photon. Only photon with energies higher than the band gap energy of the material are absorbed. In 1954, Chapin *et al.* were the first ones to build a PV device based on mono-crystalline silicon (*c*-Si) with an energy conversion efficiency of ~6 % [3]. Nowadays, the record for *c*-Si based solar cells is 25.0 % [4].

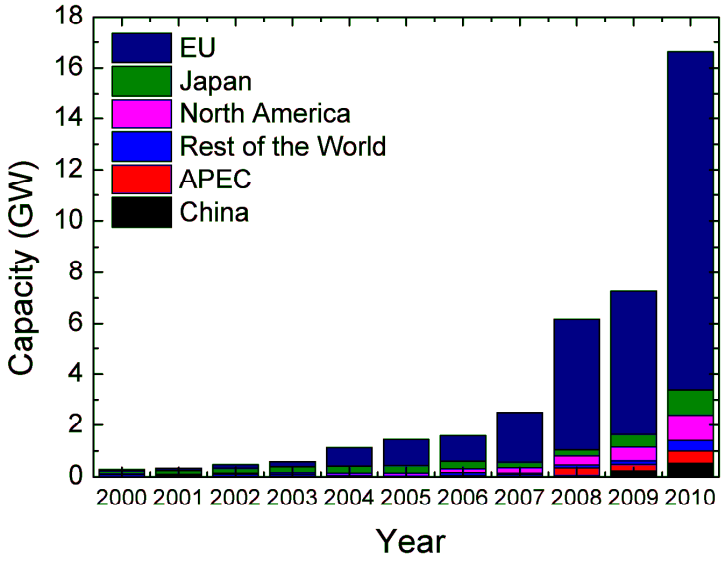

Figure 2: Global annual PV capacity of installed instalations [1].

Due to its band gap energy, which enables silicon to absorb photons with energies down to 1.1 eV, silicon is a common used material for photovoltaic devices. Other well-known materials for photovoltaic devices are a-Si:H, CdTe and CuIn(Ga)Se_2. All these materials have a band gap between 1.0 and 2.5 eV, depending on material and deposition characteristics. Since the production of silicon is an expensive process, dominance of other materials (e.g. CuIn(Ga)Se_2) was expected. However, nowadays the PV market is still dominated by silicon based photovoltaic devices [5,6]. Figure 3 shows a crystalline silicon market share of around 80 % in 2012.

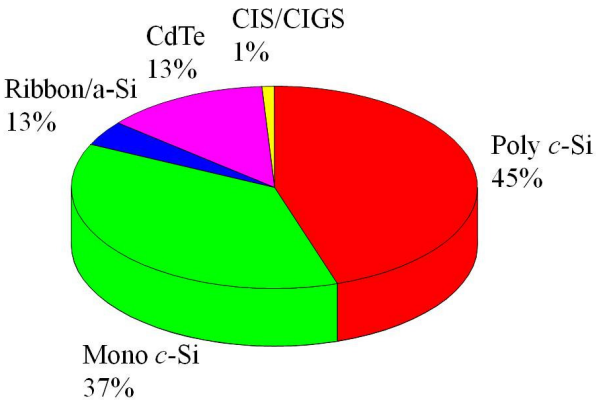

Figure 3: Photovoltaic technologies shares in 2012 [6].

1.3. *c*-Si solar cell

As shown in Figure 3, the PV market is dominated by silicon based photovoltaic devices. Expected is that the silicon dominance will last at least until 2020 [7]. In order to maintain this market share of silicon in PV technology and obtain grid parity (the moment that the price (cost/kWh) of energy generated by a renewable energy source is equal to the price of energy generated by conventional power sources) production costs of silicon based PV modules require a significant cost reduction. In the PV market, two trends are observed to reduce the cost/kWh: (i) reduction of the module costs and (ii) improvement of the conversion efficiency. Figure 4 shows the PV module production costs for silicon based devices [1].

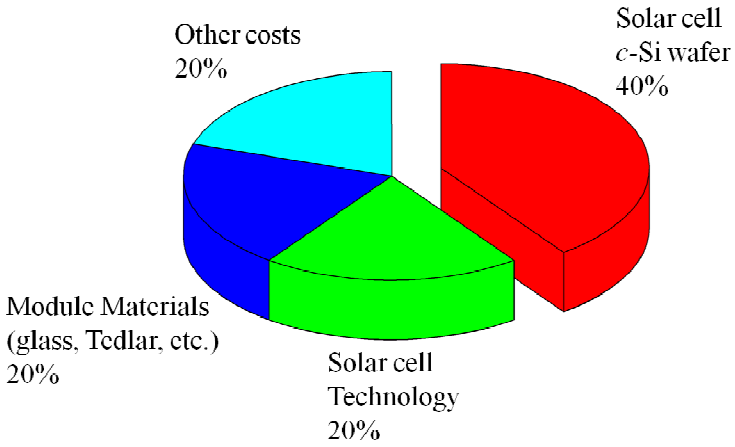

Figure 4: Production costs of a silicon based PV module [1].

As depicted in Figure 4, 40 % of the module production cost is determined by the silicon wafer. The search for alternative production of silicon (less sensitive to impurities) and the reduction of the silicon thickness are technological developments used to reduce the silicon cost price. Nowadays the solar cell industry uses (less pure and less expensive) solar grade Czochralski

(CZ) silicon for the production of solar cells. The typical thickness of mono-crystalline solar cells is 200 μm. *c*-Si solar cells costs can be further reduced by decreasing the *c*-Si substrate thickness. A further decrease of the silicon thickness comes together with other technological challenges; (i) the production and handling of thinner *c*-Si wafers, (ii) improvements of light trapping properties, (iii) avoidance of wafer bow, (iv) development of a contactless metal contact for thin silicon wafers and (v) good surface passivation of front and rear of the solar cell [8]. This work will focus on the passivation of CZ *c*-Si substrates in order to be able to scale down the substrate thickness.

1.4. *c*-Si surface passivation

As described in Section 1.3, the passivation of the *c*-Si front and rear is one of the main technological challenges in order to reduce the thickness of the *c*-Si substrate. The passivation mechanism and the importance of the passivation layer will further be explained in Section 2.4
Aluminum Oxide (Al_2O_3) layers deposited by Atomic Layer Deposition (ALD) have been reported to provide an excellent level of *c*-Si surface passivation [9,10]. Furthermore, low deposition temperature, excellent control of thickness and excellent uniformity makes the dielectric layer extremely suitable as passivation layer in Passivated Emitter and Rear Cell (PERC) *c*-Si solar cells. Therefore, in this work, Al_2O_3 layers are used to passivate *c*-Si surfaces.

1.5. Motivation

The passivation quality of Al_2O_3 passivation layers is determined by (i) the *c*-Si surface finishing (ii) material characteristics and (iii) post-deposition thermal treatment [9-11]. As described above, the goal of the thin film is to passivate surfaces in PERC *c*-Si solar cells. The production of PERC *c*-Si surface cells requires (high temperature) thermal treatments (as will be explained in Section 2.1). These thermal treatments affect the material, layer and thereby, the passivation properties of the dielectric layer. Furthermore, it has been reported that a post-deposition thermal anneal is required for an excellent level of surface passivation [9-11]. A full overview of material and layer characteristics of as-deposited and thermal treated passivation layers has not been reported yet. Therefore, the aim of this work is to gain insight in material, layer and passivation properties of Al_2O_3 layers before, during and after a thermal treatment. This insight is used to optimize the passivation quality of Al_2O_3/a-SiN_x:H stacks (this is a typical rear passivation stack used in *c*-Si solar cells, as will be explained in Section 2.1). The optimized passivation stacks are integrated into PERC *c*-Si solar cells.

The first part of this work gives an overview of the effect of a thermal treatment on the fixed charge density, surface defect density, atomic concentration, crystal phase structure, film stress, interface properties and surface defects of Al_2O_3 films on *c*-Si substrates. Using the overview from the first part, the passivation quality of Al_2O_3/a-SiN_x:H stacks will be optimized. In the last part, the optimized passivation layer will be used as rear passivation layer in PERC *c*-Si solar cells. The solar cells will be characterized and compared to cell characteristics of industrial PERC solar cells.

2. *c*-Si solar cell and *c*-Si surface passivation

Introduction

As described in the introduction, the goal of this work is to give an overview of the effect of a thermal treatment on the material, layer and passivation properties of Al_2O_3 films in order to optimize the passivation quality of the Al_2O_3 films. The optimized layer will be integrated into *c*-Si solar cells. As described in Section 1.5, the passivation quality is significantly influenced by the post-deposition thermal treatment. This Section will describe the production process of a *c*-Si solar cell to highlight the thermal treatments required for the manufacturing of this type of solar cells. These treatments will be applied on the passivation layer in order to evaluate the effect of the treatment. Furthermore, the passivation mechanism of a thin functional layer will be explained. Finally, a list of possible passivation layers and their suitability is given.

2.1. *c*-Si solar cell production sequence

Nowadays, most of the industrially produced *c*-Si solar cells are full aluminum (Al) Back-surface-field (Al BSF) solar cells because of their simplicity and low production costs. As depicted in Section 1.3, 40 % of the total production costs are determined by the *c*-Si substrate and, therefore, in order to achieve grid parity, one should reduce the *c*-Si substrate thickness. However, in case of the full Al BSF *c*-Si solar cell, two fundamental problems are observed upon decreasing the substrate thickness (i) conversion efficiency is reduced due to low effective carrier lifetimes (this will be further explained in Section 2.3) and (ii) strain formed at the Si-Al interface causes the wafer to bow considerably [12]. Both problems are the main drive to develop the Passivated Emitter and Rear Contacted (PERC) solar cells, where the full Al rear contact is replaced by a passivating dielectric layer to enhance the effective carrier lifetime. In case of industrial PERC (i-PERC) solar cells, high quality SiO_x layers are used as rear passivation layers. Semiconductor-metal contacts are formed through localized openings in the dielectric layer. Figure 5 shows a schematic overview of a full Al BSF and an *i*-PERC cell. In this work, both the full Al BSF and *i*-PERC solar cells are used as a reference cells. The typical production process of an *i*-PERC cell based on *p*-type mono-crystalline Silicon (*c*-Si) is displayed below. Full Al BSF solar cells can be produced by using an equivalent scheme without step 6, 7 and 9.

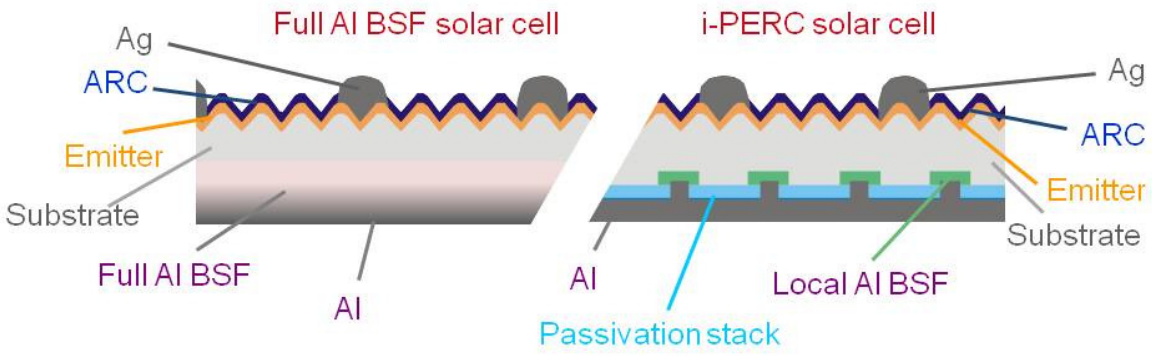

Figure 5: Schematic overview of a full Al-BSF solar cell (left) and i-PERC solar cell (right). The production process and the function of each element is explained in the text below.

1. *Saw Damage Removal* (SDR). Slicing of the wafers results in a high amount of surface defects, typically 10-15 µm thick. The damaged layers are removed by an alkaline solution (KOH or NaOH) at 80 ˚C for 10 min.

2. *Front side texturing*. A pyramidal surface is created to reduce front side reflectance. Random pyramids are formed on both sides in an alkaline solution (with additives).

3. *Rear side polishing.* Rear side polishing is needed in order to enhance the internal reflectance and to reduce rear side recombination. For the polishing, an acidic solution is used in a single-side wet-bench tool.

4. *Phosphorous diffusion.* Phosphorous Oxide is deposited on the wafer and then the phosphorous is driven into the substrate in order to create the n^+ emitter regions. $POCl_3$ and O_2 gasses are used to form a Phosphorus-silica glass (PSG) layer (P_2O_5) on the substrate, from which the phosphorus can diffuse into the wafer substrate at 850 ˚C.

5. *PSG and single-side emitter removal.* The PSG layers are removed from the back side by a HF based solution. In order to avoid the bipolar transistor effect, the n^+ emitter is removed from the back by a HF based solution in a single-side wet-bench tool.

6. *Rear side SiO_2 deposition.* A high quality SiO_2 layer is thermally grown (at 1050 ˚C) on the back for surface passivation. A forming gas anneal (H_2/N_2 mixture at 350 ˚C) is needed to achieve a high level of surface passivation.

7. *Rear side silicon nitride (a-SiN_x:H) deposition.* a-SiN_x:H is deposited on top of the SiO_2. The high density of the dielectric creates a barrier against Al spiking. Another advantage is that the hydrogen in the film is beneficial for the surface passivation; it further reduces the amount of surface defects furthermore (the mechanism will be explained in Section

2.4). 100 nm of a-SiN_x:H is deposited at 400 ˚C by Plasma Enhanced Chemical Vapor Deposition (PE-CVD) using SiH_4 and NH_3 precursors.

8. *Front side a-SiN_x:H deposition.* a-SiN_x:H layer is deposited on the front of the substrate as Anti-Reflection Coating (ARC) and emitter passivation. Absorption depends on the refractive index and the thickness of the dielectric. Typically a layer with a refractive index of 2.0 and a thickness of ~100 nm is deposited.

9. *Rear side laser ablation.* The dielectric stack is locally ablated by a nano-second laser to create vias to form semiconductor-metal contacts. A dot pattern with a pitch size of 50 ± 10 μm is used to minimize the contacts coverage. Typically, 1.47 % of the rear stack is opened for contacting [13].

10. *Rear side Al deposition.* Aluminum (Al) is deposited on top of the rear dielectric stack for contacting and back reflection purposes. The back layer can be deposited by evaporation (thermal or e-beam) or by screen-printing an Al containing paste on the back. The screen-printing technique uses a squeegee pressing the printable material over a mask.

11. *Front side silver (Ag) screen-printing.* The screen-printing method is used to manufacture the front contacting grid. The grid is optimized to minimize the shadowing losses while ensuring enough current capacity [12].

12. *Co-firing.* The substrates received a Rapid Thermal Anneal (RTA) at a peak temperature of typically 860 ˚C (so-called co-firing). The final production step is performed using an industrial available belt furnace. On one hand, front contacts are formed thanks to the penetration of the Ag through the ARC layer during the RTA, and on the other hand, the rear side Al penetrates into the *c*-Si creating a heavily doped p^{++}, the so called local back surface field (BSF), also used for contacting.

Full Al-BSF solar cells can be produced by using the sequence as described above without steps 6, 7 and 9. Using this process, a semi-conductor metal contact and a heavily doped p^{++} region will be formed on the full rear of the solar cell.

i-PERC solar cells with efficiencies ~18 % can be obtained using *c*-Si substrates with a thickness of 160 – 180 μm (see Section 3.3.1). Full Al BSF *c*-Si solar cells with conversion efficiencies close to 17 % can be processed from equivalent substrates (Section 3.3.2).

One expects that passivation quality is most influenced by the final co-firing step; therefore, this thermal treatment will be applied on the rear passivation stack.

2.2. *c*-Si surface finishing

As described in the introduction, one of the parameters that influence the passivation quality is the *c*-Si surface finishing prior to deposition of the passivation layer. One can distinguish two different surface finishes, the hydrophobic and the hydrophilic surface finishing. In case of the hydrophobic surface finishing, the *c*-Si surface is –H terminated while in case of the hydrophilic surface finishing, the *c*-Si surface is –OH terminated. Both *c*-Si surface states can be prepared using a wet-chemical process. The cleaning process for the preparation of *c*-Si substrates with hydrophilic surfaces is displayed in Table 1.

Table 1: Cleaning sequence of *c*-Si substrate. The *c*-Si will be oxidized during the final cleaning step.

	Solution	*Temperature*	*Time*
1	H_2O + HF (2 %) + HCl (5 %)	Room temperature	5 min.
2	H_2O_2 + H_2SO_4 (1:4)	± 80 ˚C	10 min.
3	H_2O + HF (2 %) + HCl (5 %)	Room temperature	5 min.
4	NH_4OH + H_2O_2 + H_2O (1:1:5)	Room temperature	10 min.

The hydrophobic *c*-Si surface finishing can be obtained by performing step 1-3. In between the clean steps and at the end of the cleaning procedure, the wafers are cleaned by rinsing in deionized water. After the last rinse, the substrates are dried in a hot-air or a Maragoni dryer. The hydrophilic surface finishing is more stable over time, however it takes longer to prepare the surface state and the residuals of the cleaning solution may probably decrease the conversion efficiency of the final cell. In this study both surface finishes are used to investigate the effect of the cleaning on the final cell results.

2.3. Recombination losses

As depicted in the Section above, a passivation layer is deposited on the surfaces of the *c*-Si substrates. The layer is grown on the *c*-Si surface to enhance the solar cell conversion efficiency. This increase in efficiency can be understood by the fact that the solar cell efficiency is influenced by the time between the formation of an electron-hole pair and the recombination of the pair [8]. The time between formation and recombination is expressed by the effective minority carrier lifetime. The minority carrier can be either an electron or a hole, depending on the dominating carriers in a specific substrate (electrons are the minority carriers in *p*-type *c*-Si and the holes in *n*-type *c*-Si). The excited electron/hole needs a certain time to diffuse either to the front or to the rear, where it is collected. If the excited electron/hole recombines before it reaches the rear/front, the number of collected electron/holes decreases and, therefore the conversion efficiency decreases as well. By depositing a passivation layer on the *c*-Si surface, the effective minority carrier lifetime is enhanced.

This can be understood because the effective minority carrier lifetime contains a contribution of both the bulk and the surface minority carrier lifetime; therefore, the effective minority carrier lifetime can be expressed by Equation (1):

$$\frac{1}{\tau_{eff}} = \frac{1}{\tau_{bulk}} + \frac{1}{\tau_{surface}} \quad (1)$$

With τ_{eff} the effective minority carrier lifetime, τ_{bulk} the bulk minority carrier lifetime and $\tau_{surface}$ the surface minority carrier lifetime.

The bulk minority carrier lifetime is determined by:

- Radiative recombination losses
- Auger recombination losses
- Shockley, Read, Hall recombination losses

The first two loss mechanisms are intrinsic recombination processes and the last one is an extrinsic recombination process. Figure 6 displays a schematic overview of the recombination loss mechanisms.

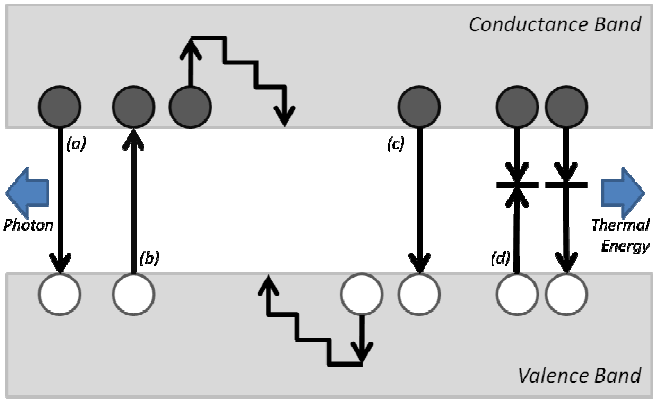

Figure 6: Schematic overview of intrinsic (a-c) and extrinsic (d) recombination losses. (a) radiative recombination, (b) Auger recombination by transferring the energy to an electron in the conductance band, (c) Auger recombination by transferring the energy to a hole in the valance band and (d) SRH recombination.

The intrinsic losses are dominated by two unavoidable mechanisms: radiative and Auger recombination. In the case of radiative recombination, an excited electron in the conductance band recombines and emits a photon. Auger recombination is a three-body process, where an electron and a hole recombine by transferring the energy to another electron/hole. The probability of radiative losses is low due to the indirect band gap of *c*-Si. However, since Auger recombination is a three-body process, Auger losses reduce the effective minority carrier bulk lifetime at high injection levels significantly. The injection level is the minority carrier density in non-equilibrium (illuminated). Both radiative and Auger recombination losses reduce the bulk minority carrier lifetime. However, the dominant bulk recombination mechanism for most *c*-Si wafers is the extrinsic recombination via defect states. Impurities and *c*-Si dangling-bonds create bulk defect states in the *c*-Si band gap. Electrons and holes can recombine via these interband

states by releasing thermal energy. The recombination processes via interband defect states has been described by Shockley, Read and Hall (SRH) [14].

Furthermore, as displayed by Equation (1), the effective minority carrier lifetime is influenced by the surface minority carrier lifetime. The surface minority carrier lifetime is significantly lower than the bulk minority carrier lifetime. This can be understood because the *c*-Si surface is an extreme disruption of the crystal structure, resulting in a high density of *c*-Si dangling bonds at the surface. These dangling bonds create interband defect states and thereby enhance electron-hole recombination tremendously. The surface effective minority carrier lifetime can be approximated by Equation (2) [15]:

$$\frac{1}{\tau_{surface}} = \frac{2S_{eff}}{W} \tag{2}$$

S_{eff} is the effective surface recombination velocity and W the substrate thickness.

2.4. Passivation mechanism

Equation (1) shows that the effective minority carrier lifetime is determined by the bulk and the surface minority carrier lifetime. Furthermore Equation (2) shows that the surface minority carrier lifetime increases linearly with the substrate thickness. The bulk minority carrier lifetime is a material property, and is not influenced by the substrate thickness. However, the surface minority carrier lifetime, and therefore the effective carrier lifetime, depends linearly on the substrate thickness. For thin films, the bulk effective minority carrier lifetime can be neglected and the effective minority carrier lifetime is dominated by the (significantly lower) surface minority lifetime.

In order to enhance the surface minority carrier lifetime and therefore the effective minority carrier lifetime, one should reduce the surface recombination velocity as much as possible [16]. The surface recombination velocity depends on the interface defect density (the number of possible recombination points) and the minority carrier concentration (more carrier accessible for recombination). Therefore, one can reduce the effective surface recombination velocity by two different strategies: (i) reducing the interface defect density and (ii) reducing the surface minority carrier concentration [16].

The interface defect density can be reduced significantly by the formation of Si-H, Si-O or Si-N bonds, reducing the number of dangling bonds (and hereby reducing the interband states) at the surface. The formation of these bonds is called chemical passivation. The passivation bonds can be formed by the deposition of a thin functional film (e.g. high quality SiO_2, a-SiN_x:H, Al_2O_3) on the surface of the *c*-Si substrate or by a forming gas treatment (the substrate is heated in a H_2 environment).

Furthermore, the effective surface recombination velocity can be decreased by reducing the electron or hole concentration at the surface. One can reduce the electron or hole concentration by creating an internal electric field below the interface. The creation of an internal electric field

is called field-effect passivation. An electric field can be created by fixed charges at or close to the surface of the substrate, providing a potential barrier for electrons or holes to reach surface. The internal field can be obtained by a doping profile below the *c*-Si surface or by the presence of electrical charges at the semiconductor interface.

2.5. Thin functional films

As described above, thin functional films can be used to improve the surface passivation. On one hand, thin functional films decrease the interface defect density by the passivation of dangling *c*-Si bonds, and on the other hand, fixed charges in the layer can create an internal electric field and thereby reduce the minority carrier concentration. It has been suggested that the conversion efficiency of *c*-Si solar cells is enhanced by improving the effective minority carrier lifetime, however, the efficiency improvement is also determined by the optical properties and the thermal stability of the thin function film [8]. For front side passivation, the thin film needs to be transparent to sunlight irradiation and the reflection of the sunlight needs to be reduced. On the rear, the layer has to function as a reflection layer in order to enhance the absorption probability of the transmitted light in the silicon bulk. The optical properties are determined by the refractive index and the extinction coefficient. Furthermore, thermal stability of the thin function film is required, since, local back surface field are formed during a rapid thermal anneal (Section 2.1). Table 2 given an overview of the materials that have been suggested or used to improve thin *c*-Si solar cells. The Table also depicts the suitability of the optical properties [8].

Table 2: Functional thin films which have been suggested to improve the conversion efficiency once applied in *c*-Si solar cells.

Material	Optical properties		Surface passivation			
	Front	*Rear*	*p-type*	*p^+-type*	*n-type*	*n^+-type*
TiO_2	++	++	--	--	?	?
Therm. SiO_2	+	++	++	+	++	++
PECVD SiO_2	+	++	+/-	?	+/-	?
a-SiN_x:H	++	++	+	-	++	++
a-Si:H	-	-	++	+	++	++
AlF_3	+	++	+/-	?	?	?
Al_2O_3	+	++	++	++	++	?

a-SiN_x:H and SiO_2 are thin functional films that have been used successfully as passivation layer and/or anti-reflection layer in *c*-Si solar cells, due to their excellent chemical passivation. Both thin film are used as passivation layer in *i*-PERC solar cells (see Section 2.1). Nevertheless, a field-effective passivation for *p*-type *c*-Si substrate is not provided by the positive fixed charges present in the a-SiN_x:H and SiO_x passivation layer [17]. Electrons are the minority carriers in *p*-type *c*-Si; therefore, fixed negative charges are preferred.

It has been proven that Al_2O_3 proved an excellent level of surface passivation on *c*-Si substrates, due to, on one hand, the high fixed negative charge density, providing the field-effective passivation, and on the other hand, excellent chemical passivation [9,10]. Especially the high

negative fixed charge density makes the thin film extremely suitable as rear passivation layer in *p*-type *c*-Si solar cells. Therefore, Al_2O_3 layers will be characterized to determine the potential of the thin functional layers as rear passivation layer in *p*-type *c*-Si solar cells.

3. Surface Passivation Experiments and Results

3.1. Characterization of Al_2O_3 layers

Introduction

As described in Section 2.4, Al_2O_3 layers have been proven to provide an excellent level of *c*-Si surface passivation [9,16,18,19] The passivation mechanism of Al_2O_3 on *p*-type *c*-Si surfaces has been reported to be governed by two mechanisms; chemical passivation of the surface defects and field effect passivation by negative fixed charges providing a potential barrier for electrons to reach the *c*-Si/Al_2O_3 interface [16]. It has been reported that the interface defect density and the formation of fixed negative charges are influenced by a post-deposition thermal treatment [9]. Furthermore, Al_2O_3 structural changes are commonly observed during a thermal treatment [20]. The aim of this section is to evaluate the properties of Al_2O_3 films after different thermal treatments. Post-deposition anneals at different temperatures are applied on the passivation layers. Table 3 gives an overview of the techniques used to characterize the Al_2O_3 films before and after the thermal treatments. The parameter that is evaluated using the measurement technique is also depicted in Table 3. Al_2O_3 layers are deposited on *c*-Si substrates using a thermal Atomic Layer Deposition (ALD) process at 200 ˚C in a Cambridge Nanotech Savannah S200 using TriMethyl-Aluminum (TMA) and H_2O. Both the hydrophilic and the hydrophobic *c*-Si surface finishing prior to the deposition of the Al_2O_3 layers have been used.

Table 3: Overview of the characterization techniques and the extracted parameters.

Section	*Characterization Technique*	*Parameter*
3.1.1	Capacitance-Voltage (CV) measurements	D_{it} and Q_{eff}
3.1.2	Elastic Recoil Detection (ERD)	Atomic density
3.1.3	Temperature Desorption Spectroscopy (TDP)	Species desorption
3.1.4	Fourier Transformed Infrared spectroscopy (FTIR)	Atomic bonds
3.1.5	X-Ray Diffraction (XRD)	Phase transitions
3.1.6	Bowing measurement by laser scanning	Film stress
3.1.7	Optical surface inspection	Blistered area

3.1.1. Capacitance-Voltage (CV) measurements

In this Section, the mobile charge density, fixed charge density and the interface trap density of Al_2O_3 layers deposited on *c*-Si after different thermal treatments will be evaluated using Capacitance-Voltage (C-V) measurements.

Al_2O_3 layers with a thickness of 5 - 20 nm are deposited on the front of Saw Damage Removed (SDR) *p*-type CZ *c*-Si with a resistivity of 1.5 Ω·cm and a thickness of 150 μm. Prior to deposition, *c*-Si surfaces are -H or oxygen-terminated by the cleaning processes described in

Section 2.1. On the rear, aluminum is deposited using magnetron sputtering deposition. After aluminum deposition, the passivation layers received a post-deposition anneal at temperature varying from 300 to 900 ˚C in N_2 environment for a time interval of 20 minutes. Platinum dot electrodes with an area of $(2.0 \pm 0.5) \times 10^{-3}$ cm^2 were evaporated on top of the Al_2O_3 layers. C-V curves from -3 to 3 V are recorded using an HP 4156 precision LCR-meter and at low and high (1 – 100 kHz) frequency. All measurements are carried out at room temperature.

Figure 7 displays C-V curves of 10 nm Al_2O_3 after a N_2 anneal at different temperatures.

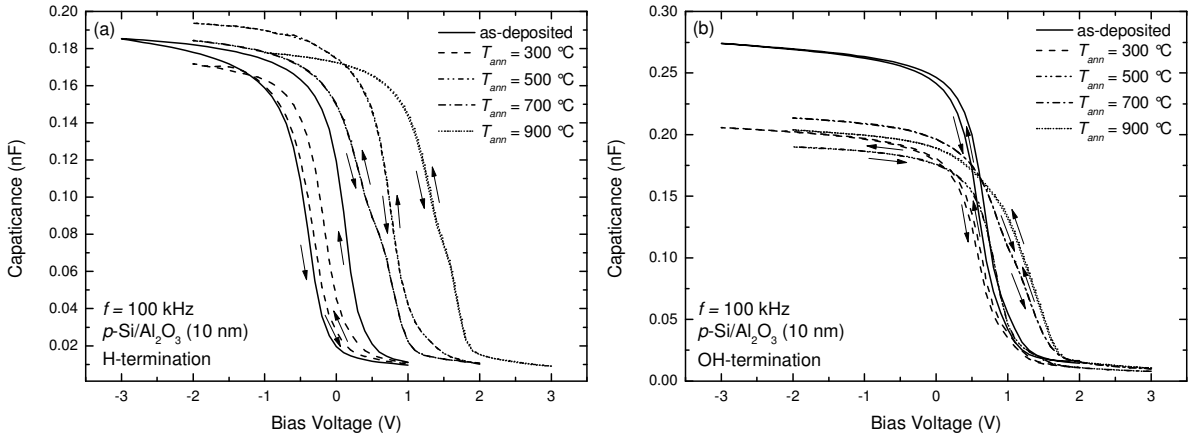

Figure 7: Capacitance-Voltages curves measured on Al/*c*-Si/Al_2O_3 capacitor after a N_2 anneal at a temperature diplayed in the Figure. (a) 10 nm Al_2O_3 on *c*-Si surfaces with H-termination and (b) on *c*-Si surface with OH-termination.

The as-deposited and samples annealed at T_{ann} = 300 ˚C demonstrate counterclockwise hysteresis (difference between the flat-band voltage toward positive bias and the flat-band voltage towards negative bias, the flat-band voltage is the value with the highest slope) during the bias voltage sweep. The hysteresis has been observed for both *c*-Si surface finishes, and indicates the presence of mobile charges in the dielectric [21]. The mobile charges (Q_m) are due primarily by the presence of ionic impurities like K^+, Na^+, Li^+ and H^+. Mobile charges density (Q_m) is quantified using Equation (3) [21].

$$Q_m = -\Delta V_{fb} C_{ox} \tag{3}$$

With ΔV_{fb} the difference in flat-band voltage between the forward and the backward bias voltage sweep and C_{ox} the oxide capacity (capacitance at -3 V). The mobile charge density of 10 nm thick Al_2O_3 layers on *c*-Si with hydrophobic or hydrophilic surfaces is displayed in Table 4.

Table 4: Mobile charges density in 10 nm thick Al_2O_3 layers deposited on *c*-Si surfaces with H- or OH-termination, annealed at different temperatures.

	Hydrophobic	Hydrophilic
T_{ann} (˚C)	Q_m ($\times 10^{-12}$ cm^{-2})	Q_m ($\times 10^{-12}$ cm^{-2})
As-dep	125.1	15.7
300	36.0	4.7
500	3.1	4.7
700	11.6	14.9
900	2.2	7.2

Table 4 shows that the mobility charge density is influenced by the *c*-Si surface finishing; before annealing, mobile charge densities of 125.1 $\times 10^{-12}$ and 15.7 $\times 10^{-12}$ cm^{-2} are reported in Al_2O_3 layers on *c*-Si with hydrophobic or hydrophilic surface finishing respectively. For both *c*-Si surface states, the mobile charge density is reduced after a thermal anneal (3.1 $\times 10^{-12}$ and 4.7 $\times 10^{-12}$ cm^{-2} for hydrophobic and hydrophilic *c*-Si surface finishing respectively after a N_2 anneal at 500 ˚C). At an annealing temperature of 700 ˚C, mobile charge densities increase slightly for both *c*-Si surface states.

It is most likely that mobile charges are caused by H^+ coming from the H_2O and TMA precursor, used to grow the dielectric layer. As-deposited amorphous layers contain a high concentration of H, as will be shown in Section 3.1.2. The high mobile charge density in Al_2O_3 layers on hydrophobic *c*-Si surfaces before annealing indicates the presence of higher H^+ concentration. The hydrogen concentration is higher than the equivalent passivation layer on H-terminated *c*-Si surfaces. It has been hypothesized that the difference is caused by the higher amount of hydrogen present on the *c*-Si surface prior to the deposition of the Al_2O_3 layer. During the thermal anneal, hydrogen is released from the dielectric, resulting in a decrease of mobile charges. Section 3.1.3 will show that hydrogen is released for both surface finishes. It has been hypothesized that the increase of the mobile charge at T_{ann} = 700 ˚C is caused by the effusion of H from the *c*-Si substrate. Beyer *et al.* reported a high effusion rate of hydrogen from bare *c*-Si substrates at 625 ˚C, indicating a high breakage rate of Si-H bonds [22]. The increased breakage of Si-H bonds results in an increase of H+ radicals, and thereby an increase of the mobile charge density in the Al_2O_3 layer. Furthermore, at higher annealing temperatures, the H^+ radicals are outgassed from the Al_2O_3 layers leading to a decrease of the mobile charges.

The fixed charges density (Q_f) in the dielectric layer is determined using Equation (4).

$$V_{fb} = \phi_{MS} - \frac{Q_f d}{\varepsilon_r \varepsilon_0} \tag{4}$$

Where V_{fb} is the flat-band voltage of the forward bias voltage sweep, *d,* the oxide thickness, ϕ_{MS} is the metal-semiconductor work function difference and ε_r the dielectric constant, which can be calculated by given by Equation (5) [21]:

$$\varepsilon_r = \frac{C_{ox} d}{A} \tag{5}$$

With A, the dot electrode area and ε_0 vacuum permittivity. Using Figure 7, an electric permittivity of $\varepsilon_r = 9 \pm 1$ can be calculated. This value is reasonable for Al_2O_3 thin films and consistent with previous reports [23].
Q_f can be determined from the linear fit of the V_{fb} as a function of the Al_2O_3 thickness. The slope of the fit is equal to $Q_f d / \varepsilon_r \varepsilon_0$, and intercept with the y-axis represents ϕ_{MS}. Using the film thickness and the electric permittivity, one can calculate the fixed charge density. The fixed charge density in Al_2O_3 layers on hydrophobic c-Si surface is displayed in Figure 8.

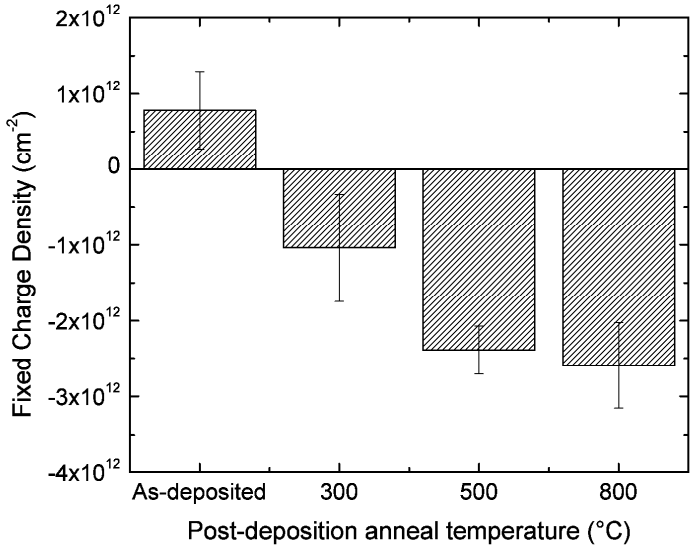

Figure 8: Fixed charge density in Al_2O_3 layers deposited on c-Si with hydrophobic surface finishing as a function of the annealing temperature.

A positive fixed charge density of $Q_f = + (0.8 \pm 0.5) \times 10^{11}$ cm^{-2} is reported for as-deposited Al_2O_3 layers. After a post-deposition anneal at $T_{ann} = 300$, negative fixed charges with a density of - $(1.1 \pm 0.5) \times 10^{12}$ cm^{-2} are formed. Annealing the samples at 500 ˚C and 800 ˚C results in a negative fixed charge density of - $(2.5 \pm 0.5) \times 10^{12}$ and - $(2.6 \pm 0.6) \times 10^{12}$ cm^{-2} respectively.
It has been suggested that the high H concentration results in a positive charge density. During the post-deposition treatment, hydrogen is detached from –OH groups, creating negatively charged oxygen interstitials in the bulk Al_2O_3 [16]. The thermal treatment is needed to break the –OH bonds in as-deposited Al_2O_3. Increasing the annealing temperature leads to breakage of more –OH bonds, and therefore, a higher negative fixed charge density.

The interface defect density can be evaluated using the conductance of the dielectric. An approximate expression given the interface defect density in terms of the measures maximum conductance is [21].

$$D_{it} \approx \frac{2.5}{q}\left(\frac{G_p}{\omega}\right)_{\max} \qquad (6)$$

With q the magnitude of the electron charge, G_p the maximum conductivity and $\omega = 2\pi/f$ (f the frequency). The impact of the anneal temperature on the interface defect density of Al_2O_3/c-Si structures is shown by Figure 9. The Figure shows both the hydrophobic and the hydrophilic c-Si surface state prior to the deposition of the 10 nm thick Al_2O_3 layer.

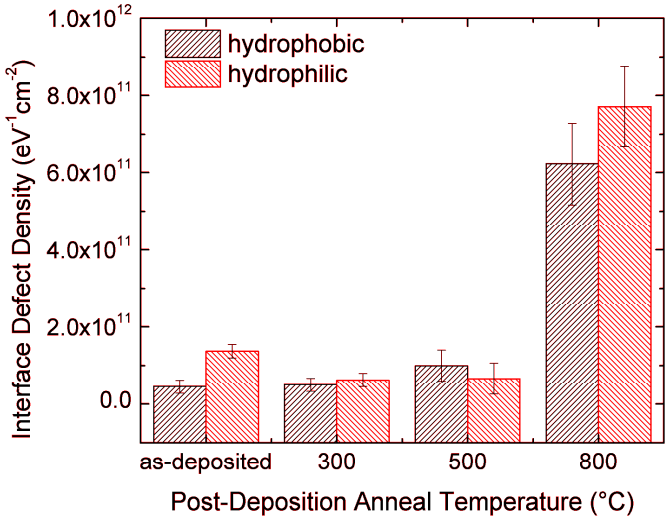

Figure 9: The effect of the annealing temperature on the D_{it} of Al_2O_3/c-Si structures. Both the hydrophobic and the hydrophilic c-Si surface state prior to the deposition of the 10 nm thick Al_2O_3 layer are displayed.

Figure 9 depicts that a low interface defect density (D_{it} = (4 ± 1) ×10^{10} $eV^{-1}cm^{-2}$ and (13 ± 1) ×10^{10} $eV^{-1}cm^{-2}$ for hydrophobic and hydrophilic c-Si surface finishes respectively) are obtained by depositing 10 nm thick Al_2O_3 layers on the c-Si surfaces. After an anneal at T_{ann} = 300 ˚C, an interface defect density of D_{it} = (4 ± 1) ×10^{10} $eV^{-1}cm^{-2}$ (hydrophobic) and (6 ± 1) ×10^{10} $eV^{-1}cm^{-2}$ (hydrophilic) is obtained. At T_{ann} = 800 ˚C, the interface defect density increases for both c-Si surface conditions to (7.5 ± 1.0) ×10^{11} $eV^{-1}cm^{-2}$ in case of the hydrophobic surface state and (7.2 ± 1.0) ×10^{11} $eV^{-1}cm^{-2}$ for the hydrophilic surface state prior to the deposition of the Al_2O_3 layer.
A low interface defect density has been obtained by depositing an Al_2O_3 layer on the c-Si substrate due to the formation of Si-O and Si-H bonds. Si-O bonds are formed by depositing the thin functional film on the substrate and the hydrogen is provided by the precursors (TriMethyl-Aluminum (TMA) and H_2O) used for the deposition of the passivation layer. For as-deposited Al_2O_3 layers, higher interface defect densities have been observed in Al_2O_3/c-Si structures with the c-Si in the hydrophilic surface state compared with the hydrophobic surface state. It has been suggested the difference is caused due to the presence of a low quality (x < 2) SiO_x interfacial layer between the Al_2O_3 layer and the hydrophilic c-Si surfaces; the oxygen vacancies in the interface layer lead to a high amount of dangling Si bonds. After the thermal treatment, a high quality ($x \approx SiO_x$) interfacial layer is formed between Al_2O_3 layer and c-Si surface for both

surface states, resulting in an equivalent level of chemical passivation. The thickness is equivalent for both surface *c*-Si finishes (this will be further explained in 3.1.4). The amount of Si-O bonds increases for the samples with the hydrophilic surface finishing prior to deposition. The formation of the interfacial layer will be evaluated in section 3.1.4. As suggested above, annealing the samples at high (> 800 ˚C) temperature leads to the breakage of Si-H bonds [24]. The breakage of Si-H bond results in a decrease of the level of chemical passivation, depicted by an increase of the interface defect density.

In conclusion, Figure 10 shows both the D_{it} and Q_f of Al_2O_3/*c*-Si structures before and after annealed. The samples are annealed at different temperature, as depicted in the Figure.

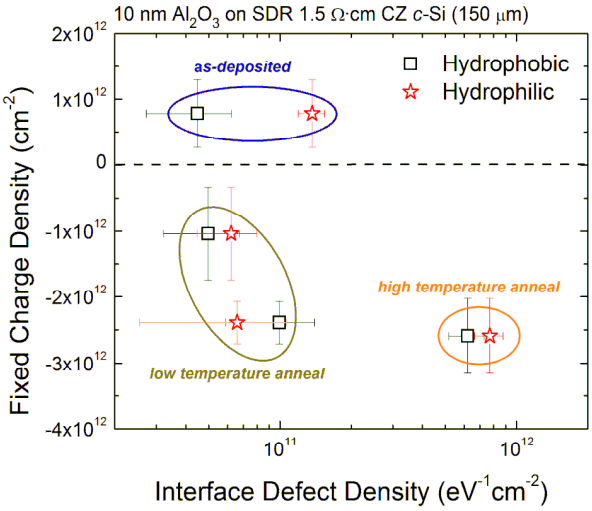

Figure 10: Interface defect density and fixed charge density of as-deposited, low temperature (≤ 500 ˚C) annealed and high temperature (> 500 ˚C) annealed Al_2O_3 samples deposited on hydrophilic and hydrophobic *c*-Si surfaces.

Figure 10 shows clearly the effect of a thermal treatment; a fixed charge density with positive polarity is measured in as-deposited Al_2O_3 films, after a low (≤ 500 ˚C) temperature thermal treatment, negative fixed charges are formed. Annealing the samples at high (> 800 ˚C) temperature results in an increase of the negative fixed charges, however, the interface defect density increases significantly because of the depletion of hydrogen from the Al_2O_3/*c*-Si interface.

3.1.2. Elastic Recoil Detection (ERD)

In Section 3.1.1, it has been suggested that hydrogen effuses from the Al_2O_3 layers during the thermal treatment. Elastic Recoil Detection (ERD) is used to characterize the atomic density of Al_2O_3 layers before and after thermal annealing. 100 nm thick layers Al_2O_3 are deposited on both sides of 2.72 Ω·cm FZ *p*-type mirror polished *c*-Si with a thickness of 285 µm. One sample received a post-deposition thermal anneal at 600 ˚C in N_2 environment for 20 minutes. Both samples are analyzed by ERD. The atomic densities of Aluminum (Al), Oxygen (O) and Hydrogen (H) are determined and displayed in Table 5.

Table 5: Atomic density of 100 nm as-deposited and annealed (N_2, 600 ˚C, 20 min.) Al_2O_3 layers measured by ERD.

Sample	[Al] (at. %)	[O] (at. %)	[H] (at. %)	[O]/[Al]
Al_2O_3 as-deposited	37.45	60.52	2.03	1.62
Al_2O_3 annealed	38.47	60.82	0.72	1.58

As depicted in Table 5, a hydrogen concentration of 2.03 atomic % is present in the as-deposited Al_2O_3 layer, while the concentration decreased to 0.72 atomic % after a post-deposition thermal anneal, proving that hydrogen effuses during the thermal treatment. The results are similar to values reported in literature [25]. The ratio [O]/[Al] has decreased to 1.58 after the thermal treatment.

Figure 11 shows the hydrogen profile of the Al_2O_3 layers before and after annealing.

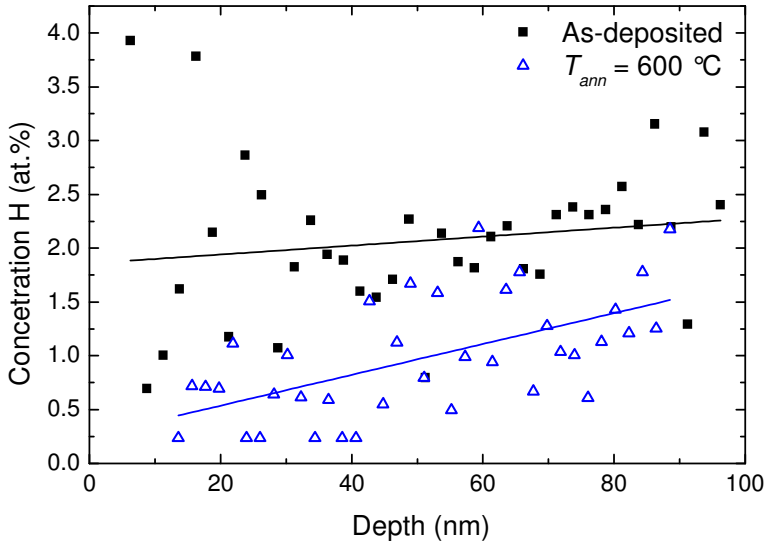

Figure 11: Hydrogen profile of 100 nm thick Al_2O_3 layers before and after annealing (N_2, 600 ˚C, 20 min.). On the x-axis is the layer depth with $x = 0$, the Al_2O_3 surface and x = 100 the *c*-Si/Al_2O_3 interface. The black and the blue line are a guide to the eye.

Before annealing, the hydrogen is uniformly distributed in the Al_2O_3 layer, as demonstrated by the black line. During the thermal anneal, hydrogen is released from the dielectric, as shown in Table 5. The monotone increasing line in Figure 11 indicates that less hydrogen is present at the Al_2O_3 surface than in the region close to the Si/Al_2O_3 interface. Al_2O_3 is known to be an effective gas diffusion barrier, limiting the diffusion of hydrogen and/or hydrogen containing fragments, leading to gradient in the hydrogen concentration [26]. Furthermore, Si-H bonds break as a consequence of the increased thermal energy, resulting in the depletion of hydrogen from the *c*-Si substrate [24]. This hydrogen diffuses into the Al_2O_3 layer resulting in a higher hydrogen concentration at the region at the Al_2O_3/*c*-Si interface.

3.1.3. Temperature Desorption Spectroscopy (TDS)

As depicted in Section 3.1.2, hydrogen is released during a thermal treatment. In this Section, the effusion of hydrogen, oxygen and carbon containing fragments from Al_2O_3 layers during a thermal treatment will be investigated by Temperature Desorption Spectroscopy (TDS). 5 nm thick Al_2O_3 layers are deposited by ALD on both sides of 4" mirror polished *p*-type CZ *c*-Si with a resistivity of 2 Ω·cm and a thickness of 160 µm. Prior to deposition, the hydrophobic or hydrophilic *c*-Si surface finishing is obtained by the cleaning process as described in Section 2.1. The samples are placed in an ultra high vacuum reaction chamber with a base pressure of $< 10^{-6}$ bar and the samples are heated at a constant heating rate of 60 ˚C·min^{-1} up to 900 ˚C. A quadrupole mass spectrometer detects the species that desorbed from the sample at elevated temperatures. Figure 12 depicts the thermal effusion transients of the majority species released from 5 nm thick Al_2O_3 on *c*-Si with either the hydrophobic or the hydrophilic surface state. The transient were construction recording the mass numbers of the majority species (H_2, H_2O and CO_2).

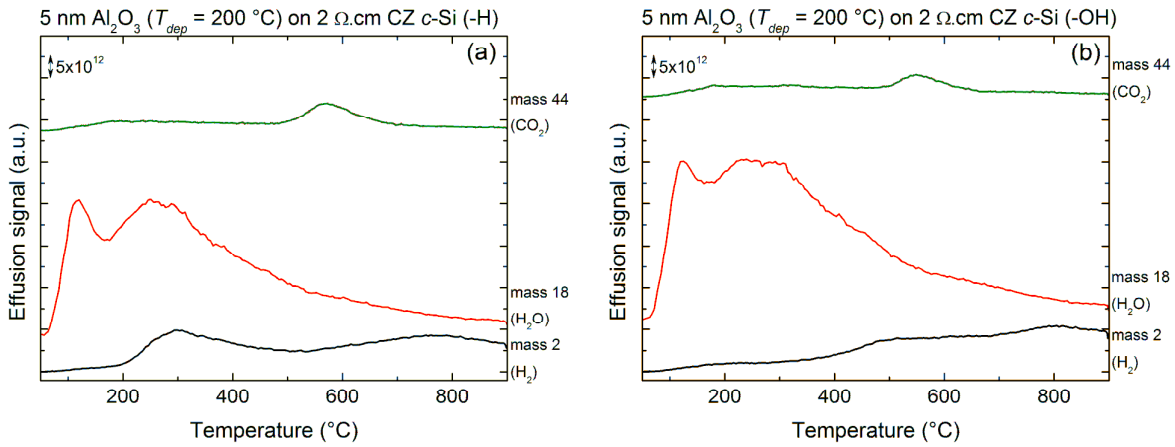

Figure 12: Thermal effusion transient at mass-over-charge ratios 2, 18 and 44 of 5 nm Al_2O_3 deposited at 200 ˚C on both sides of *c*-Si with (a) hydrophobic and (b) hydrophilic surfaces. The most likely parent molecules contributing to the signal at the selected mass-to-charge ratios have been determined. The transients are offset for clarity.

The effusion transients of 5 nm Al_2O_3 on *c*-Si with hydrophobic surfaces are displayed in Figure 12 (a). Transient of H_2 shows an effusion peak at 300 ˚C and 800 ˚C. The effusion transient of H_2O has an intense peak at 100 and 275 ˚C. At 575 ˚C, an effusion peak is observed in the transient corresponding to release of CO_2.

Figure 12 (b) displays the thermal effusion transients of the majority species released from 5 nm Al_2O_3, deposited on both sides of *c*-Si with hydrophilic surface finishing. The effusion signal of H_2 demonstrates a maximum at 500 and 800 ˚C. The H_2O effusion rate is at the maximum at 100 ˚C and 275 ˚C. The signal corresponding to CO_2 species shows a maximum at 550 ˚C.

Furthermore, the effusion of species is investigated by calculating the integral of the thermal effusion transients in Figure 12. The integral corresponds with the amount species effused during the thermal treatment. The result is displayed in Figure 13.

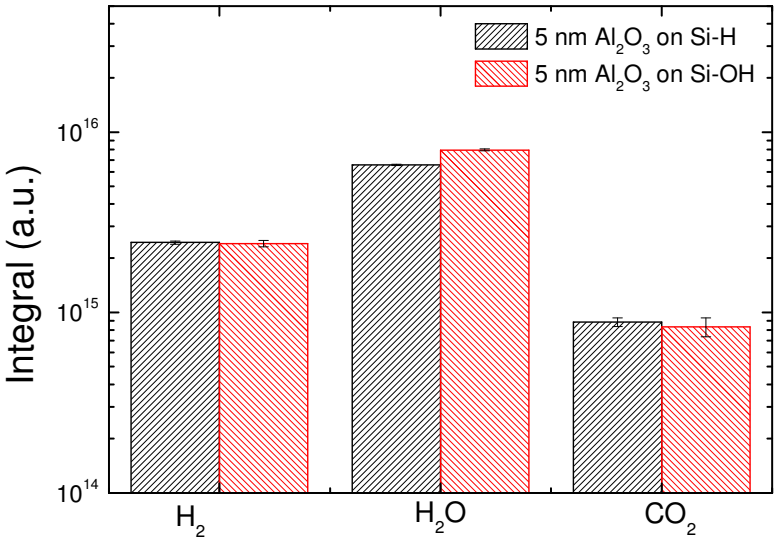

Figure 13: Integral of the thermal effusion transients (correspond to the majority species released from Al_2O_3 passivation layers), as depicted in Figure 12. The integral is calculated from 50 to 900 ˚C.

Slightly more H_2O is released from the Al_2O_3 layer deposited on hydrophilic *c*-Si surfaces. An equivalent amount of H_2 and CO_2 is released from both samples.

The effusion of H_2 and H_2O is consistent with the presence of –OH groups in the Al_2O_3 bulk. It has been suggested that the peak at 100 ˚C in the effusion transient of H_2O is caused by the outgassing of residuals of the H_2O precursor used for manufacturing the passivation layer. At higher temperature, H and HO groups are released from the Al_2O_3 layer, forming H_2O and H_2. The highest formation rate of H_2O has been observed at 300 ˚C.
Both the effusion spectra of H_2 show two peaks (for the hydrophobic surface finishing 300 and 800 ˚C and the hydrophilic surface finishing peak are observed at 500 and 800 ˚C). It has been hypothesized that the first peak is caused by the effusion of H coming from the Al_2O_3 layer and the second peak is caused by effusion of H from the *c*-Si substrate. It has been reported that a high amount of Si-H bonds break at 600 ˚C and due to the gas diffusion barrier effect of the Al_2O_3 layer limiting the diffusion of species, a peak at 800 ˚C arises in the transient [24]. It has been assumed that the temperature difference of the first peak as well the difference in H_2O effusion is caused by the limited sensitivity; however, more insight is needed to confirm this theorem.
Furthermore, the formation of CO_2 indicates the incorporation of impurities, coming from the TMA precursor, during the deposition of the dielectric.

3.1.4. Fourier Transform Infrared spectroscopy (FTIR)

It has been suggested that a low-quality SiO_x interfacial layer is present between the Al_2O_3 and the hydrophilic *c*-Si surfaces and that a high-quality SiO_x interfacial layer is formed during a thermal treatment for both *c*-Si surface finishes. In this section Fourier Transform Infrared

Spectroscopy (FTIR) will be used to evaluate the structural properties of Al_2O_3 samples and to investigate the SiO_x interface layer [27].

Al_2O_3 layers (30 nm) are deposited on 4" mirror polished *p*-type FZ *c*-Si with a resistivity of 2 Ω·cm and a thickness of 200 µm. Prior to deposition, the *c*-Si surfaces are H-terminated or oxidized, by the cleaning process described in Section 2.1. The samples received a post-deposition anneal at a temperature (T_{ann}) varying from 300 to 900 ˚C for 20 minutes in N_2 environment. The FTIR spectrum from 400 to 4000 cm^{-1} is measured using a Bruker IR spectrometer. All the measurements are carried out at room temperature.

The absorbance spectra of Al_2O_3 samples are displayed in Figure 14. Expected bonds in amorphous Al_2O_3 and the wave number range of the IR absorption peaks are shown in Table 6 [28].

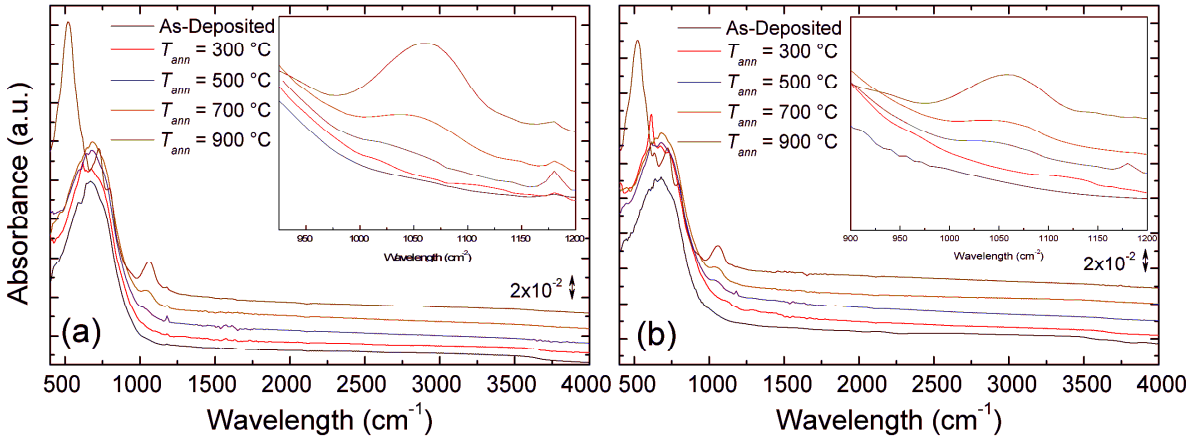

Figure 14: Absorption spectrum of Al_2O_3 deposited on *c*-Si with (a) H-terminated and (b) oxidized surfaces. The black line is the spectrum of as-deposited Al_2O_3. The red, blue, green and dark red are the spectra of Al_2O_3 after a post-deposition anneal (N_2, 20 min.) at respectively 300, 500, 700 and 900 ˚C. The spectra are off set for clarity.

Table 6: Infrared absorption band assignments from the literature [28].

Assignment	*Wave number (cm^{-1})*	*Reference*
AlO_6	400-530	[29]
O-Al-O	650-700	[20,30-32]
Al-O	750-850	[20,27,30-32]
Si-O (TO) & O-Si-O (stretch)	1060	[24,30]
Al=O	1345	[30]
CH_3 (asym. deformation) or O-CH_3	~1475	[33-35]
O-C-O	1550-1595	[33-36]
C=O	1620	[32,35,36]
O-H (stretch)	2600-3500	[32-34,36]

The broad features that appear between 450 and 1000 cm^{-1} are characteristic for aluminum oxide; O-Al-O and Al-O bonds are characterized by absorption peaks between 650-700 and 750-850 cm^{-1} respectively. The spectra of Al_2O_3 deposited on *c*-Si with hydrophobic or hydrophilic surfaces show equivalent Al-O features. The range from 2500 – 4000 cm^{-1} is characterized by the IR absorption of OH groups.
After the post-deposition N_2 thermal anneal, an absorption peak at 1060 cm^{-1} appears in the FTIR spectrum, indicating that a SiO_x interface layer is formed between the Al_2O_3 layer and *c*-Si surfaces. The peak increased as a function of the annealing temperature. Furthermore, the absorption by OH groups decreases after annealing. The absorption spectrum of Al_2O_3 shows an increased absorption peak at 530 cm^{-1}, after a thermal anneal at T_{ann} = 900 ˚C.

The effect of the post-deposition anneal is even more visualized by a differential spectrum between as-deposited and annealed (500 ˚C, 20 minutes) Al_2O_3 samples. The differential spectrum is displayed in Figure 15.

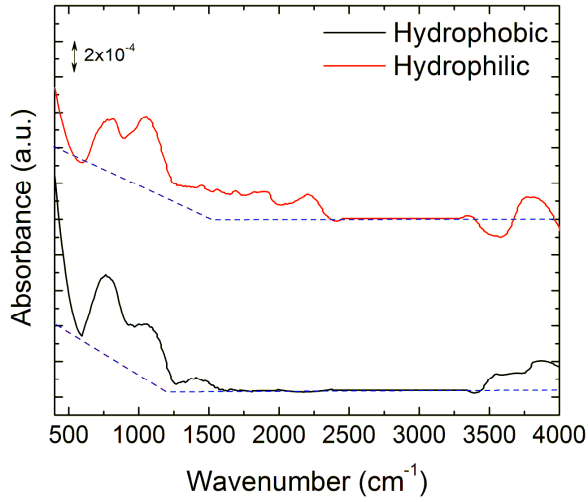

Figure 15: Differential absorption spectrum between as-deposited films and N_2 annealed (N_2, 500˚ C, 20 min.) samples. Peaks in the spectrum indicate structural changes induced by a thermal anneal. The red and the black line represent the differential spectrum of a 30 nm thick Al_2O_3 on c-Si with hydrophilic and hydrophobic surface finishing respectively. The blue line is the expected base-line. Spectra are off set for clarity.

Figure 15 has been constructed by dividing the absorption spectrum of annealed (N_2, 500 ˚C, 20 minutes) Al_2O_3 samples by the absorption spectrum of an as-deposited Al_2O_3 samples. Due to a lack of knowledge about the exact baseline, the expected baseline is sketched in Figure 15. Peaks above or below the baseline indicate an increase or decrease of the specific bond respectively. One can assign peaks in the spectrum by using Table 6 and data reported in Section 3.1.2 and 3.1.3.

By inspecting the differential absorption spectra and using Table 6, one can conclude that peaks at 750 and 1050 cm^{-1} indicating a change in AlO_6, Al-O and Si-O bonds respectively.

Furthermore, a change in –OH groups is observed in both spectra, indicated by a peak at 3500 cm^{-1}.
Using the absorption spectra (hydrophilic and hydrophobic), one can conclude that as-deposited Al_2O_3 are characterized by a high amount of -OH groups. As expected in Section 3.1.3, –H and –OH groups are detached during a thermal treatment indicated by a decreased absorption at 3500 cm^{-1}. The amount of Al-O and O-Al-O bonds increases thanks to the effusion of –H. This has been visualized by a peak in the differential spectrum at 750 cm^{-1}. The high peak at 530 cm^{-1} is caused by IR absorption of AlO_6 octahedra, indicating the phase transition from the amorphous to the γ-Al_2O_3 crystal phase [29]. Crystal phase transition will be further investigated in Section 3.1.5.
Peaks at 1060 cm^{-1} in both absorption spectra indicate the formation of a SiO_x interfacial layer. The intensity increases as a function of the annealing temperature. The formation of the SiO_x interface layer will be further investigated in the following Section.

To evaluate the difference between both *c*-Si surface finishes, the differential spectrum between Al_2O_3 deposited on *c*-Si with H-terminated or oxidized surface has been constructed. The spectrum of an Al_2O_3 deposited on hydrophilic *c*-Si is divided by the spectrum of an equivalent layer on hydrophobic *c*-Si surface. The expected baseline is displayed in the Figure. Peaks above the baseline indicate enhanced absorption by the Al_2O_3 layer on hydrophilic *c*-Si surfaces. Both spectra are displayed in Figure 16.

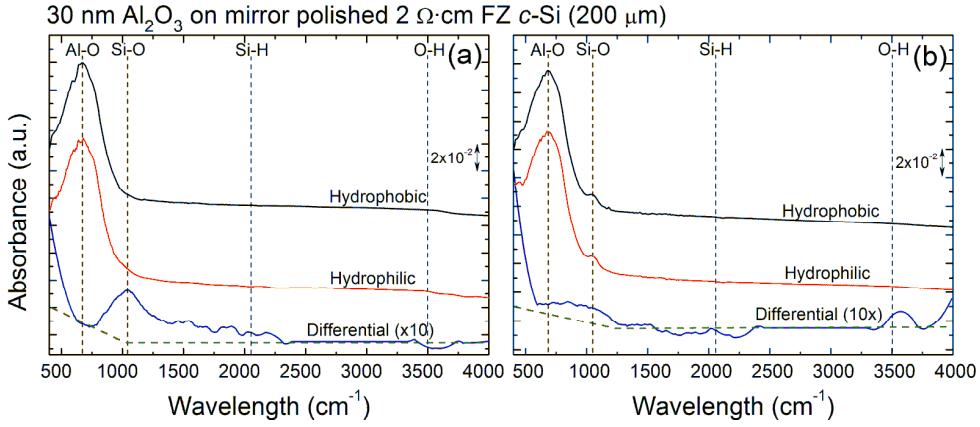

Figure 16: Infrared absorption spectra of 30 nm Al_2O_3 deposited on both sides of *c*-Si with hydrophobic or hydrophilic surfaces. The differential absorption spectrum is displayed to indicate the difference between the passivation layers. (a) The spectrum of as-deposited Al_2O_3 layers and (b) after a post-deposition anneal (N_2, 20 min. at 700 ˚C). The green line is the expected base-line. Spectra are off set for clarity.

For as-deposited Al_2O_3, the difference in surface finishing is demonstrated by an absorption peak at 1060 cm^{-1} indicating absorption by Si-O bonds. No significant difference is visible for the absorption peak associated with Si-H bonds. After the post-deposition anneal, a SiO_x interface layer was formed for both samples, indicated by the absence of an absorption peak at 1060 cm^{-1}.

Figure 16 displays that the amount of SiO_x bonds is higher in as-deposited Al_2O_3 layers on hydrophilic c-Si surfaces compared with equivalent layers on hydrophobic c-Si surfaces. From this one can conclude that the thickness of the SiO_x interfacial layer is influenced significantly by the *c*-Si surface finishing; depositing Al_2O_3 layers on *c*-Si in the hydrophilic surface state results in significantly thicker interfacial layers compared to equivalent layers on *c*-Si in the hydrophobic surface state. SiO_x layers of equivalent thickness have been observed after annealing. SiO_x interfacial layers of equivalent thickness are formed during the thermal treatment, as suggested in Section 3.1.1.

As described above, Si-O bonds cause an absorption peak at 1060 cm^{-1} in the FTIR spectrum. In order to determine the SiO_x interfacial thickness after a thermal treatment, 30 nm thick Al_2O_3 films are grown on both sides of 4" mirror polished *p*-type FZ *c*-Si with a resistivity of 2 Ω·cm and a thickness of 200 µm capped by a thermal grown SiO_x layer with varying layer thickness. The SiO_x layer thickness is varied by etching 100 nm thick, high quality, thermal grown (1050 ˚C) SiO_x layers using a buffer HF solution. The thickness is determined by Spectroscopic Ellipsometry (SE) (SENTECH SE400adv-PV) prior to Al_2O_3 deposition. The FTIR spectra of $Al_2O_3/SiO_x/c$-Si structures with 30 nm thick Al_2O_3 and varying SiO_x thickness are constructed and the absorbance at 1060 cm^{-1} as a function of the SiO_x thickness is plotted in Figure 17.

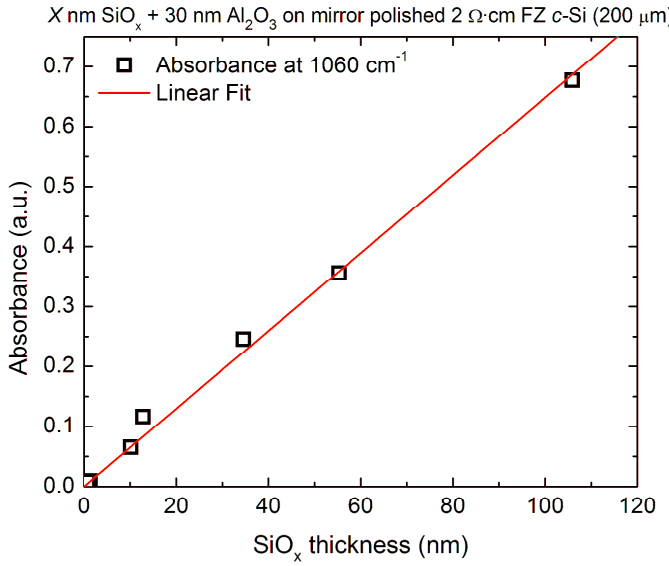

Figure 17: Absorbance at 1060 cm^{-1} of the $Al_2O_3/SiO_x/c$-Si samples a function of the SiO_x thickness. The SiO_x thickness has been measured by SE prior to the deposition of the 30 nm thick Al_2O_3 layer by ALD.

As displayed in Figure 17, the absorbance at 1060 cm^{-1} depends linearly on the SiO_x thickness. This can be understood, since, FTIR spectra apply to Lambert-Beer's law, which a relation for the absorbance is given by Equation (7).

$$-\ln\left(\frac{I}{I_0}\right) = \alpha l \qquad (7)$$

With I the transmittance intensity of the sample, I_0 the absorbance of the reference sample (bare c-Si), the α absorbance coefficient and l the thickness. Equation (7) shows that the logarithm of the absorption divided by the absorption of the reference sample depends linearly on the transmittance length. Therefore, Figure 17 can be used to determine the thickness of the SiO_x after a thermal treatment, using the assumption that the quality of the SiO_x interlayer is equal to the quality of the thermally grown SiO_x layer. The linear fit shows that $\alpha = (6.5 \pm 0.1) \times 10^{-3}$ nm^{-1}. Using Equation (7) and Figure 17, one can calculate that a SiO_x interface of 2.0 ± 0.2 (hydrophilic) and 1.7 ± 0.2 nm (hydrophobic) is formed during a post-deposition anneal at 700 ˚C.

3.1.5. X-Ray Diffraction (XRD)

Al_2O_3 films deposited at low temperature are amorphous; however, they may crystallize during a thermal treatment [37]. The transition from the amorphous to a crystalline state significant influences the electrical properties of the dielectric, even more; the volume reduction induced by a phase transition increases the film stress, and can result in blister formation (blister formation will be described in Section 3.1.7) [38,39]. In this Section, the phase transition of Al_2O_3 layers, induced by the thermal treatment, is investigated by X-Ray Diffraction measurement (XRD).

The phase diagram of aluminum oxides and aluminum hydrides is illustrated in Figure 18 [38].

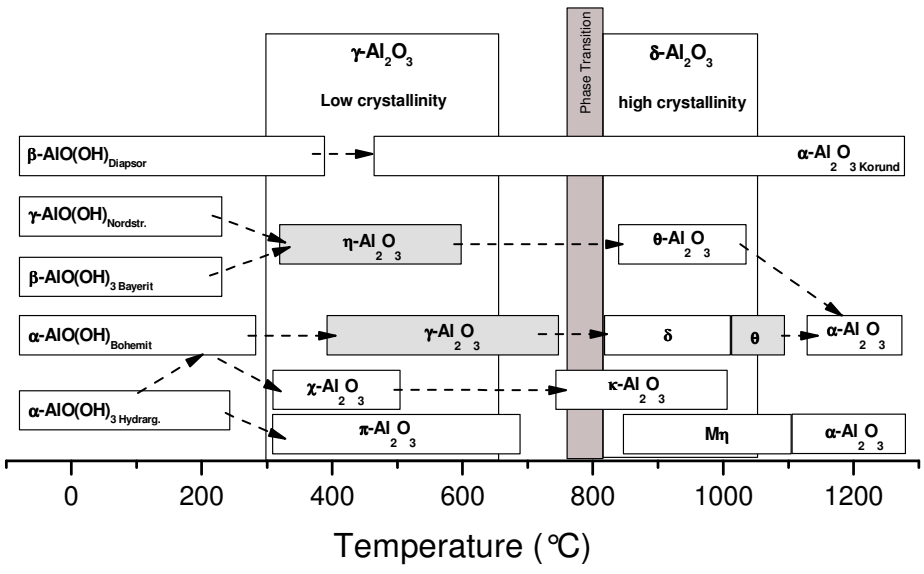

Figure 18: Phase diagram of Aluminum oxides and Aluminum hydrides [38].

In Figure 18, it can be seen that Al_2O_3 has many (meta) stable crystal states. Figure 18 displays various phase transitions; typically phase transitions take place around 800 ˚C, depending on

deposition method, (post-) deposition condition and film characteristics (e.g. thickness). For Al_2O_3 layers deposited by ALD, the initiation of phase transition from amorphous to γ-Al_2O_3 is known to occur at (750 – 800 ˚C) [37]. Table 7 gives a short overview of Al_2O_3 films before and after a thermal treatment, as reported in literature.

Table 7: Overview of phase transitions and the thermal budget

	Al_2O_3 characteristics			*Phase Transition*		*Annealing conditions*		
Author	Thickness (nm)	Dep. Method	Dep. Temp. (˚C)	Start	End	Temperature (˚C)	Time (min)	
V.V Afans'ev	10-100	ALD	300	am	γ	800	10	[37]
G. Krautheim	3 - 60	ALD	200 - 500	am	γ/θ/δ/κ	870	*	[38]
S. Jakschik	3.5 - 8	ALD	*	am	γ	900	30	[40]
P. Eklund	2,000	Sputtering	< 700	am/γ	α	900	60	[41]
S. Cava	55	Wet chem.	400	am/γ	α	800	*	[42]

* no information available

One can see that using ALD, amorphous Al_2O_3 layers are deposited. After the thermal treatment as specified in the Table, the amorphous layers transformed into crystalline γ-Al_2O_3 or a mixture of γ/θ/δ/κ –Al_2O_3 [37,38,40] Table 7 also shows the influence of the film characteristic on the thermal treatment required for the phase transition; higher annealing temperature are needed to transform thin (≤ 10 nm) as-deposited layers into crystallite films. As-deposited Al_2O_3 films in the γ phase can be manufactured using other techniques [41,42]. The alumina film transforms into α-Al_2O_3 by applying an equivalent thermal treatment used to transform amorphous Al_2O_3 into γ-Al_2O_3. This illustrates the influence of the deposition technique on the phase transition.

The crystal phase transition behavior of 5 and 30 nm thick Al_2O_3 films, grown by ALD is investigated using the Panalytical X'pert Pro MRD, performing a 2Θ grazing incident (GI) scan at a grazing angle of 10˚. The films were deposited on both sides of 2.72 Ω cm FZ *c*-Si double sided polished *p*-type wafers with a thickness of 285 μm and (100) orientation and hydrophobic surface fishing. The samples received a N_2 anneal for 20 min starting at a temperature varying from 400 ˚C up to 1000 ˚C with intermediate steps of 100 ˚C. In Figure 19, the XRD spectra of 30 nm thick Al_2O_3 layers are shown after the post-deposition treatment and after a 50 point Savtizky-Golay smoothing.

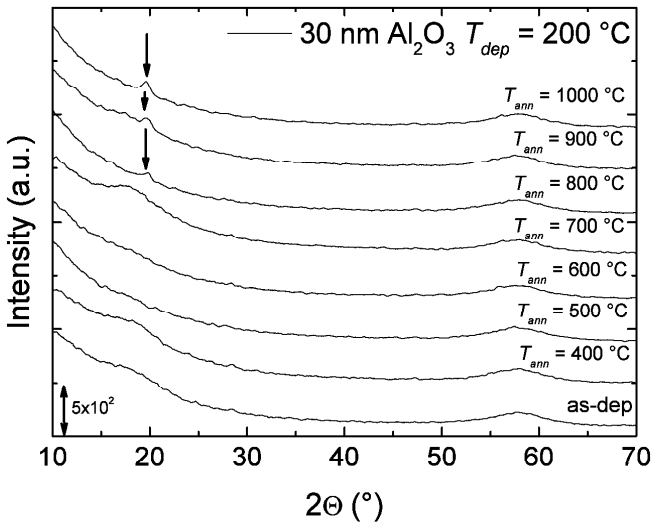

Figure 19: XRD spectra of 30 nm thick Al_2O_3 layers after a 20 min N_2 anneal at different temperatures. The spectra are offset for clarity.

In Figure 19, it can be seen that besides the broad peak at 58˚, no peaks show up in the spectrum of as-deposited Al_2O_3 layer, indicating that the film are amorphous. The broad peak in the spectrum is coming from the *c*-Si substrate [37]. Up to an anneal temperature of 800 ˚C the Al_2O_3 film remain amorphous, however, at 800 ˚C, a peak corresponding to the crystalline γ-Al_2O_3, shows up [37]. Table 7 shows an equivalent transition from amorphous to crystalline γ-Al_2O_3 in case of Al_2O_3 deposited by ALD.
The influence of the film thickness on the crystallization is illustrated in Figure 20.

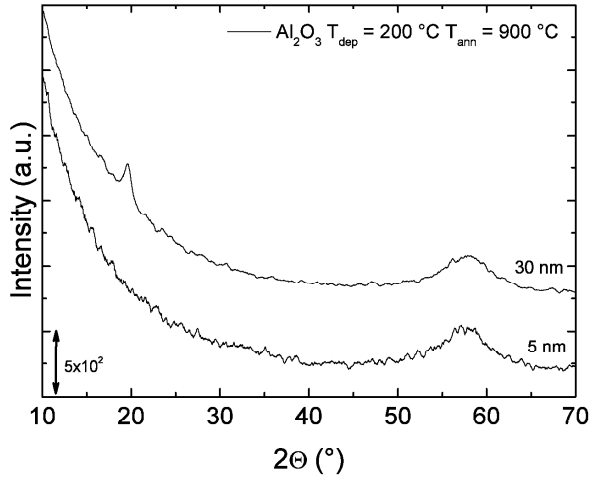

Figure 20: XRD spectra of 5 and 30 nm thick Al_2O_3 layers after an N_2 anneal at T_{ann} = 900 ˚C. The spectra are offset for clarity.

As described above, 30 nm thick Al_2O_3 films transformed from the amorphous state into the γ-Al_2O_3 phase during a N_2 anneal at T_{ann} = 900 ˚C. As expected for literature, no peaks arise in the XRD spectrum of 5 nm Al_2O_3, indicating that the layers remained amorphous after the post-deposition treatment. The thermal budget required to initiate the phase transition for thin (5 nm) films is higher.

3.1.6. Film stress

During a thermal treatment, stresses can be developed in the film and the substrate because of difference in lattice parameter or a difference in thermal expansion coefficient between the film and the substrate [39]. In this Section, the influence of the temperature on the film stress and the effect of the increased stress are investigated.

Lee *et al*. reported that under the assumption of elastic behavior and using the mass and momentum balance, the in-plain stress of a γ-phase layer can be described by Equation (8) [39].

$$\sigma^s = \frac{4E_s\varepsilon_s\ d_f}{(1-\upsilon_s)d_s} \tag{8}$$

With E_s, the Young's modulus, υ_s, the Poisson's ratio, d_f and d_s the film and substrate thickness respectively and $\varepsilon_s = e_{Si} - e_\gamma$, with e_{Si} and e_γ given by:

$$e_x = \int_{T_0}^{T} a_x dT \tag{9}$$

With a_x the thermal expansion coefficient of *c*-Si or γ-Al_2O_3, T_o and T start and ending temperature respectively. From Equation (8), one can learn that in-plane stress linear depends on thermal stress, substrate and film thickness.

The first section described the influence of the temperature on the in-plane stress under the assumption of elastic behavior; however, the induced stress can lead to spontaneous interface delamination or film fracture, depending on the energetics of the situation. If the consequent net change in energy is negative, the film undergoes spontaneous lateral deflection over the debonded region [43,44]. The deflection of the dielectric will be further evaluated in Section 3.1.7. The film is partial-delaminated to minimize the elastic energy in the substrate. The deflection of the film and therefore the release of energy is an irreversible process.

The in-plane stress in Al_2O_3 on *c*-Si is evaluated by depositing 270 nm thick Al_2O_3 layer on one side of 24 x 25 mm mirror polished *p*-type FZ *c*-Si with a resistivity of 2 Ω·cm and a thickness of 200 μm. The sample is placed in a chuck and heated up to a temperature of 400 ˚C and the bowing of the substrate is measured using a laser scanning method. The relation between the curvation (R) and the stress is given by [45]:

$$\frac{1}{R} = \frac{6\Delta T}{\left[\frac{E_s}{(1-\upsilon_s)}\right] d_s^2} \sigma^s \tag{10}$$

From this expression, the slope of the inverse curvature versus temperature measurement can be determined assuming that the expansion coefficient are independent of temperature by taking the derivative of the expression with respect to temperature [45]. This results in:

$$\frac{d\left(\frac{1}{R}\right)}{dT} = \frac{6}{\left[\frac{E_s}{(1-\upsilon_s)}\right] t_s^2} \sigma^s \tag{11}$$

Figure 21 shows the slope of the bowing, according to Equation (11) corresponding to the stress of the substrate, as a function of the temperature:

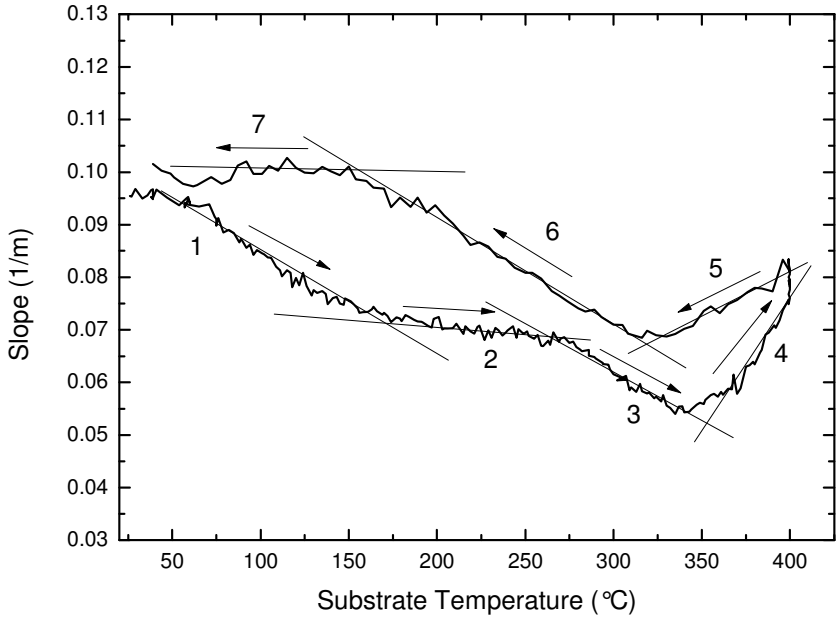

Figure 21: Temperature derivative of the bowing of a 270 nm thick Al_2O_3 layer deposited on 200 µm thick *c*-Si as a function of the temperature.

The arrows in the Figure indicate the path of heating. By inspecting Figure 21, one can see that 7 different regions can be distinguished. The first region behaves the film elastic and the strain depends linearly on the applied temperature [45]. Region two is characterized by the plastic deformation of the layer. At this temperature gaseous species effuse from the layer resulting in

structural changes, displayed by a quasi-constant stress region (see Section 3.1.3). At T = 265 ˚C once more the film behave elastic, characterized by the linear dependency of the film stress on the temperature. At T = 350 ˚C, the threshold stress value for film deflection is achieved and blistering occurs, decreasing the elastic energy in the layer. The effect of partial delamination of the film, and thereby the relaxation of the film stress, is characterized by region 4, where the stress decreases up to T = 400 ˚C. In region 5, the film is passing through a transition plastic-elastic transition until the tensile yield strength is reached [45]. Furthermore, the cooling is dominated by the elastically decrease of the film stress (region 6). At T = 150 ˚C, the last region (7) can be distinguished by a constant film stress during cooling. The irreversible energy release by the formation of blisters is depicted by a difference in start and ending point, the formation of the blisters decreased the film stress at room temperature.

3.1.7. Blistering formation

As mentioned in Section 3.1.6, the film can partial be de-laminated during a thermal treatment. Blistering is the partial de-lamination of a layer upon a thermal treatment above a critical temperature [46]. In this Section, the influence of the layer thickness and the annealing temperature on the blister formation is investigated.

As described in the introduction of this section, blistering is the partial de-lamination of a thick enough Al_2O_3 layer. Typical blisters are displayed in Figure 22 (a)-(c).

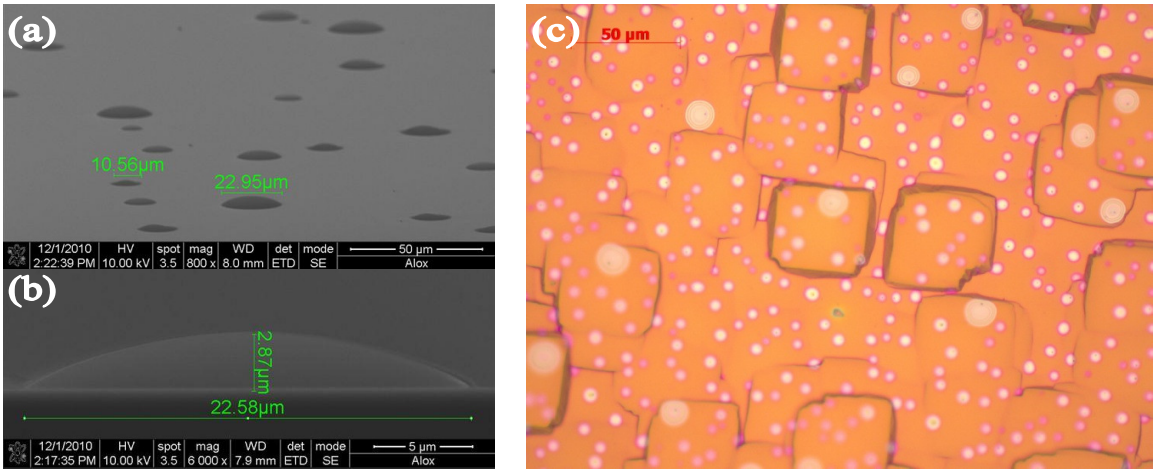

Figure 22: (a) SEM tilted top-view and (b) cross-section images of blistered ALD Al_2O_3 (60 nm) annealed at 600 ˚C deposited on mirror-polished c-Si and Figure (c) optical microscope top-view of blistered Al_2O_3/a-SiN_x:H stack (30 and 200 nm respectively) on SDR *c*-Si after co-firing.

The typically size of a blister is 1-50 µm. Figure 22 (a) and (b) show a blistered Al_2O_3 layer with a thickness of 60 nm deposited on mirror-polished *c*-Si with hydrophobic surface finishing after a N_2 anneal at 600 ˚C for 20 minutes and Figure 22 (c) the blisters surface of as-deposited Al_2O_3 (30 nm) capped with 200 nm a-SiN_x:H (deposited by PECVD at 400 ˚C) after firing. One can see in Figure 22(a) and (c) that the blisters are randomly distributed over the surface.

Figure 23 (a) and (b) show the blistered area (%) in 5, 10 or 30 nm thick Al_2O_3 layers after a thermal anneal at different temperatures. The layers are deposited on both sides of 4" Saw Damage Removed (SDR) *p*-type CZ *c*-Si with a resistivity of 2 Ω·cm and a thickness of 160 µm. Figure 23 (a) shows the hydrophobic (-H) and Figure 23 (b) shows the hydrophilic (-OH) *c*-Si surfaces states prior to Al_2O_3 deposition. The surface states are prepared using the cleaning sequence as described in Section 2.1 The Figures are constructed by inspecting the surfaces of the samples using an optical microscope. These Figures are used to determine the average size and density of the blisters at the surface.

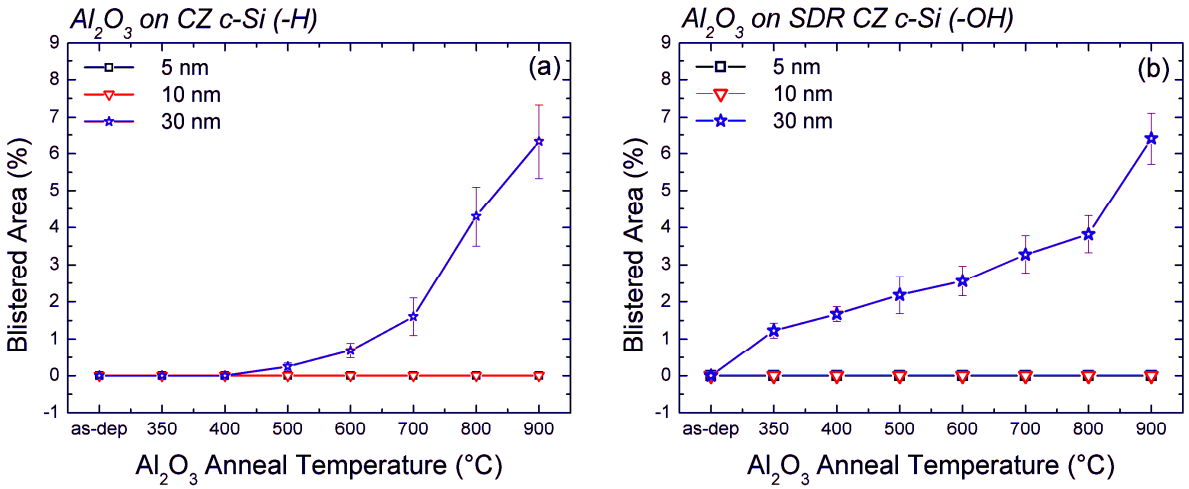

Figure 23: Blistered area (percentage of total area) as a function of annealing temperature for 5 (black), 10 (red) or 30 nm (blue) think Al_2O_3 layers deposited on *c*-Si samples with hydrophobic (a) or hydrophilic (b) surface finishing. Annealing steps are performed between 350 and 900 ˚C for 20 minutes in N_2 environment, as indicated on the horizontal axis.

Obviously, no blisters are observed in thin (≤ 10 nm) Al_2O_3 deposited on *c*-Si with either hydrophobic or hydrophilic surface finishes. Inspecting 30 nm thick Al_2O_3 films on *c*-Si with hydrophobic surface finishing (-H), it appears that blistering is initiated at an annealing temperature of 500 ˚C and the blistered area increased as a function of the annealing temperature. In case of 30 nm Al_2O_3 deposited on hydrophilic *c*-Si surfaces, blistering starts at 350 ˚C and increases as a function of the annealing temperature. An equivalent blistered area is observed after a thermal anneal at 900 ˚C for Al_2O_3 passivation layers deposited on both *c*-Si surfaces.

It has been hypothesized that the blistering formation is caused by 2 different mechanisms; (i) the capping effect of the Al_2O_3 layers prevents the effusion of H_2, H_2O and CO_2 during a thermal treatment and (ii) blisters are formed as relaxation of the film stress. As demonstrated in Section 3.1.3, H_2, H_2O and CO_2 effuse during a thermal treatment. The species are formed randomly in the dielectric. In case of thin (≤ 10 nm) Al_2O_3 layers, the species are able to diffuse to the surface and will desorb into the environment, however, in case of thick (30 nm) Al_2O_3, the dense films can acts as a barrier, preventing desorption of species. The outgassed species accumulate between the Al_2O_3 and the *c*-Si inducing a lamination of the thin film. The effusion of species depends on the temperature, as depicted in Section 3.1.3, explaining the increase of the blistered

area as a function of the temperature. Further, blistering is enhanced by the increased film stress. As one can see in Section 3.1.6, the film stress depends linearly on the film thickness (Equation (8)), and therefore, the highest film stress value is reported in 30 nm thick Al_2O_3 layers. At a threshold temperature, blisters are formed as relaxation mechanism. At high temperature, the film stress is increased by the transformation of the film structure from amorphous Al_2O_3 to the γ-Al_2O_3 crystal structure. The volume changes as a consequence of the transformation, increasing the film stress [39]. Blisters are formed as relaxation mechanism of the increased stress. Both phenomena lead to de-lamination of thick (> 10 nm) Al_2O_3 layer during a post-deposition anneal.

Figure 23 (a) shows that blistering is initiated at 500 ˚C in 30 nm thick layers while blistering formation in equivalent layers starts at 350 ˚C in Figure 23 (b). As suggested above, blistering is initiated by the capping effect of the dielectric layer. It was hypothesized that the difference can be caused by either the capping effect of the dielectric layer is larger in case of a hydrophilic c-Si surface finishing or worse adhesion of the layer to the substrate due to the interfacial SiO_x layer, however, more insight is needed to confirm this hypothesis.

Conclusion

The effect of a thermal treatment on Al_2O_3 films deposited by ALD on different *c*-Si surfaces have been investigated with the characterization techniques displayed in Table 8.

Table 8: Overview of characterization technique and the extracted parameter.

Section	*Characterization Technique*	*Extracted Parameter*
3.1.1	Capacitance-Voltage (CV) measurements	D_{it} and Q_{eff}
3.1.2	Elastic Recoil Detection (ERD)	Atomic density
3.1.3	Temperature Desorption Spectroscopy (TDP)	Species desorption
3.1.4	Fourier Transformed Infrared spectroscopy (FTIR)	Atomic bonds
3.1.5	X-Ray Diffraction (XRD)	Phase transitions
3.1.6	Bowing measurement by laser scanning	Film stress
3.1.7	Optical surface inspection	Blistered area

In this Section, it has been proven that a post-deposition anneal is required for the formation of fixed negative charges. The interface defect density of *c*-Si passivated by as-deposited Al_2O_3 layers with hydrophilic surfaces is lower compared to an equivalent layer on *c*-Si with hydrophobic surface. The difference is cause by the low quality SiO_x interfacial layer between the Al_2O_3 layer and the hydrophilic *c*-Si surface. Equivalent SiO_x interfacial layer are reported after a thermal treatment. This results in an equivalent interface defect density. The SiO_x thickness depends on the treatment temperature. During a high temperature (≥ 800 ˚C) the interface defect density increases anneal due to breakage of Si-H bonds at the interface. H_2O, H_2 and CO_2 effuse from the layer during a thermal treatment due to the detachment of -H, –OH and

carbon containing fragments. A phase transition from amorphous to the γ-Al_2O_3 crystal state has been observed in 30 nm thick Al_2O_3 layers annealed at 800 ˚C for 20 minutes in N_2 environment. 5 nm thick Al_2O_3 layers require a higher annealing temperature to initiate phase transition, therefore, 5 nm thick Al_2O_3 layers remain amorphous after a thermal anneal at 900 ˚C. Further, it has been observed that the film stress increases during a thermal treatment due to difference in thermal expansion coefficient of Al_2O_3 and *c*-Si. The film stress depends on the film thickness. Plastic deformation of the film has been characterized by a quasi-constant stress upon increasing temperature. Deflection of the thin film leads to relaxation of the film stress. Blister formation has been observed in 30 nm thick passivation layers during a thermal treatment. Blistering is partial de-lamination of the film and is caused by (i) desorption of gaseous species and (ii) the increased film stress. The Al_2O_3 is an effective gas diffusion barrier, preventing the effusion of gaseous species resulting in the formation of blisters. Furthermore, blisters are formed as film stress relaxation mechanism. Blistering formation has not been observed in thin (≤ 10 nm) Al_2O_3. The capping effect and the increased film stress are not sufficient to form blisters.

3.2. Passivation quality of Al_2O_3/a-SiN_x:H stacks

Introduction

As described in Section 3.1, material and layer properties are influenced significantly by a post-deposition thermal treatment; a post-deposition thermal treatment is required for the formation of fixed negative charges, the interface defect density (D_{it}) is affected by the SiO_x interfacial layer (formation) and the interface defect density increases after a high temperature (≥ 800 ˚C) thermal treatment caused by the release of hydrogen from the Al_2O_3/*c*-Si interface. Furthermore, the outgassing of species and the increase of film stress can result in blister formation. In this Section, the effect of a thermal treatment on layer and passivation properties of Al_2O_3/a-SiN_x:H stacks will be investigated. These stacks will be used as rear passivation stack in *i*-PERC solar cells. As demonstrated in Section 3.1.1, Al_2O_3 layers provide an excellent level surface passivation and the a-SiN_x:H is used to enhance back reflection and to provide a barrier to prevent diffusion of Al atoms into the *c*-Si during the final co-firing step. The co-firing step is required for the formation of (local) back surface fields in *c*-Si solar cells (see Section 2.1).

It has been reported that the level of passivation is influenced significantly by the final co-firing step; the high temperature treatment induces structural changes of the Al_2O_3 film and hydrogen is depleted from the *c*-Si/SiO_x interface [11]. Even more, the passivation stack may also suffer from blister formation during co-firing. In this Section, blister formation in Al_2O_3/a-SiN_x:H stacks during co-firing will be investigated. Furthermore, the effective minority carrier lifetime in *c*-Si passivated by Al_2O_3/a-SiN_x:H stacks will be evaluated. Pre-deposition wafer cleaning, Al_2O_3 layer thickness and post-deposition treatments will be varied in order to optimize the passivation stack for the integration into *c*-Si solar cells.

3.2.1. Blistering

As shown in Section 3.1.7, blisters can be formed in passivation layers, due to an increased film stress and the effusion of gaseous species upon annealing. To investigate the blistering formation in passivation stack used in *c*-Si solar cells, 5, 10 and 30 nm thick Al_2O_3 layers were manufactured on both sides of 4" Saw Damage Removed (SDR) *p*-type CZ *c*-Si wafer with a resistivity of 2 Ω·cm and a thickness of 160 µm.. These layers were thermally annealed for 20 minutes in N_2 environment at a temperature varying for 300 – 900 ˚C prior to (100 nm thick) a-SiN_x:H deposition. Finally, the samples are co-fired at 860 ˚C peak temperature using an industrial beltline furnace. The blister area is determined by inspection of the surface using an optical microscope. Figure 24 displays the blistered area of Al_2O_3/a-SiN_x:H stacks as a function of the annealing temperature with (a) the hydrophobic *c*-Si surface finishing and (b) the hydrophilic surface finishing prior to deposition of the Al_2O_3 layer.

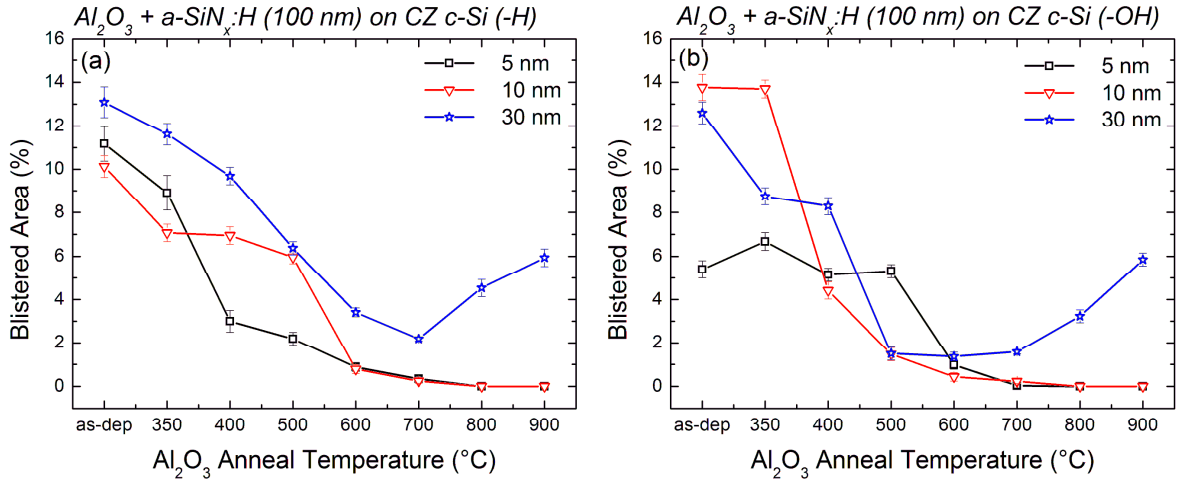

Figure 24: Blister coverage (percentage of total area) as a function of annealing temperature of an Al_2O_3/a-SiN_x:H stack with 5 (black), 10 (red) or 30 nm (blue) Al_2O_3 deposited on *c*-Si samples with (a) hydrophobic and (b) hydrophilic surface. After Al_2O_3 deposition and annealing, the samples are capped by 100 nm a-SiN_x:H and co-fired at 860 ˚C peak temperature.

One can see in Figure 24 that after co-firing, the blistered area of stacks with 5 and 10 nm Al_2O_3 is reduced as a function of the anneal temperature. No blisters are observed in stacks with 5 or 10 nm thick Al_2O_3 annealed at a temperature of ≥700 ˚C. The blistered area of passivation stacks with 30 nm Al_2O_3 shows a minimum at an annealing temperature of 700 (hydrophobic) and 500 ˚C (hydrophilic).

As described in Section 3.1.7, blistering is partial de-lamination of the passivation stack. It has been hypothesized that blistering is caused by (i) desorption of gaseous species in the Al_2O_3 layer or the *c*-Si substrate (ii) relaxation of the increased film stress.

Figure 24 shows that after co-firing, the highest blistered area is observed in the stack with as-deposited Al_2O_3 layers. This can be understood because H_2O, H_2 and CO_2 is not removed during an annealing step, therefore, a large amount of fragments are released from Al_2O_3 layers during

the co-firing. Both the capping effect and the film stress are enhanced by the a-SiN_x:H layer, consequently followed by an enhanced blister formation in the passivation stack, even with 5 nm thick Al_2O_3 layers.

The blistered area decreases as a function of the annealing temperature. In Section 3.1.3, it is made clear that the amount of H_2O, H_2 and CO_2 that is removed from the passivation layer depends on the temperature. Therefore, the effect of the high annealing temperate is that less gaseous species are removed from Al_2O_3 layers during the final co-firing step, leading to a decrease of the blistered area. Most of the gaseous species were outgassed during the annealing step prior to a-SiN_x:H deposition. No blistering is observed in stacks with 5 or 10 nm thick Al_2O_3, if the Al_2O_3 layers were annealed at a temperature of 800 ˚C or higher prior to a-SiN_x:H deposition; the outgassing of fragments prior to a-SiN_x:H deposition is sufficient to prevent blistering. Blister-free passivation stacks cannot be manufactured with 30 nm thick Al_2O_3 films. The capping effect and the film stress in thick (≥ 30 nm) Al_2O_3 layers is sufficient to form blisters, as shown in Section 3.1.7. Therefore, blistering cannot be prevented in stacks with 30 nm thick Al_2O_3 layers.

3.2.2. Al_2O_3 thickness

As described in Section 2.4, the solar cell efficiency is influenced by the effective minority carrier lifetime (τ_{eff}) in the *c*-Si. The goal of passivation layers is to enhance effective minority carrier lifetimes, and therefore, enhance solar cell efficiencies. In order to evaluate the effect of Al_2O_3 passivation layers, 5, 10 or 30 nm thick Al_2O_3 layers are deposited on both sides of 4" Saw Damage Removed (SDR) *p*-type CZ *c*-Si wafers with a resistivity of 2 Ω·cm and a thickness of 160 μm with hydrophobic surfaces. The samples are annealed in N_2 environment for 20 minutes at temperatures varying from 300 to 900 ˚C. The effective minority carrier lifetimes at an injection level of $\Delta n = 1\times10^{15}$ cm^{-3} are measured using a Sinton lifetime tester, performing Quasi-Steady-State-PhotoConductance (QSSPC) measurements in the generalized mode. An injection level of $\Delta n = 1\times10^{15}$ cm^{-3} is used because it is close to the injection level at 1 sun (1 kW m^{-2}) illumination at 25 ˚C. Subsequently, 100 nm thick a-SiN_x:H layers are deposited on top of the Al_2O_3 films. Finally, the samples are co-fired (860 ˚C peak temperature) and once more the effective minority carrier lifetime in the samples is determined by QSSPC measurements. Figure 25 depict the effective minority carrier lifetimes in *c*-Si samples passivated by a 5 (a), 10 (b) or 30 (c) nm thick Al_2O_3 layer respectively. The effective minority carrier lifetime is displayed as a function of the Al_2O_3 annealing temperature.

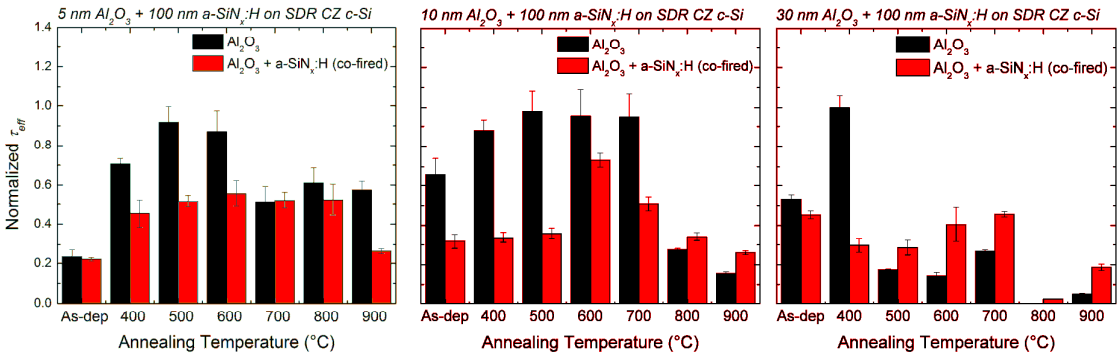

Figure 25: Effective minority carrier lifetime at Δn = 1×10^{15} cm^{-3} in *c*-Si samples with hydrophobic surfaces passivated by (a) 5 nm, (b) 10 nm and (c) 30 nm thick Al_2O_3 layers only (black) and after a-SiN_x:H capping and co-firing (860 ˚C peak temperature) (red). After Al_2O_3 deposition, the samples are annealed for 20 minutes in N_2 environment at the indicated temperature. τ_{eff} is shown as a function of the annealing temperature prior to a-SiN_x:H deposition. All lifetimes have been normalized to the highest value (113 µs).

The effect minority carrier lifetimes in *c*-Si samples passivated by an Al_2O_3 layer only (black) increase after thermal annealing. As depicted in Section 3.1.1, negative fixed charges are formed in the passivation layer during a thermal anneal, consequently follow by an improvement of the effective minority carrier lifetime. Lower lifetimes are reported after a high (≥ 800 ˚C) temperature anneal due to an increase of the interface defect density (see Section 3.1.1). The passivation quality of 30 nm thick thermally annealed (≥ 500 ˚C) Al_2O_3 layers annealed at a temperature is significantly lower compared to the 5 or 10 nm thick passivation layers. It has been hypothesized that the 30 nm thick Al_2O_3 suffer from blister formation. The fixed negative charges are removed from the interface due to blister formation (see Section 3.1.7), followed by a decrease of the effective minority carrier lifetime.

After a-SiN_x:H capping and co-firing, the highest effective minority carrier lifetime has been observed in samples passivated by 10 nm thick Al_2O_3 layers annealed at 600 ˚C prior to a-SiN_x:H capping. In case of 5 and 10 nm thick Al_2O_3 layers, the effective minority carrier lifetime in samples passivated by stacks with Al_2O_3 layers annealed at < 700 ˚C decreases after co-firing. It has been hypothesized that the effective minority carrier lifetime decreases due to an increase of the interface defect; hydrogen effuses from the interface during the high temperature treatment. Furthermore, the effective minority carrier lifetime in samples capped by Al_2O_3 layers is affected by the blister formation, removing the negative fixed charged from the interface, as hypothesized above. Especially samples annealed at low (< 600 ˚C) temperature suffer from blister formation due to the effusion gaseous species during the co-firing step. The effusion of H_2O, H_2 and CO_2 during the co-firing step results in partial de-lamination of the passivation stack. Blistering is observed in all the 30 nm Al_2O_3 stacks after co-firing, therefore, the passivation quality of stacks with thick (> 10 nm) Al_2O_3 layers is significantly lower than stacks with thin (5-10 nm) Al_2O_3 layers. The passivation quality of layers annealed at > 700 ˚C is reduced due to the high surface defect density (depicted in Section 3.1.1). This leads to the conclusion that after co-firing, the highest level of c-Si surface passivation is provide by stacks with a 10 nm thick Al_2O_3 layer, annealed at 600 ˚C prior to a-SiN_x:H deposition (τ_{eff} = 83 µs). Annealing passivation layers at

600 ˚C prior to a-SiN_x:H deposition is the best trade-off between one hand, outgassing of species to prevent blister formation during co-firing, and on the other hand, maintaining the low level of interface defect density.

3.2.3. *c*-Si surface finishing

As shown in Section 3, material characteristics, and thereby the passivation quality, are influenced by the *c*-Si surface finishing prior to deposition. Therefore, Al_2O_3/a-SiN_x:H stacks are deposited on both sides of 4" Saw Damage Removed (SDR) *p*-type CZ *c*-Si wafers with a resistivity of 2 Ω·cm and a thickness of 160 µm with hydrophilic surfaces, using the equivalent process as described in Section 3.2.2. Figure 26 depicts the effective minority carrier lifetime at $\Delta n = 1\times10^{15}$ cm^{-3} in *c*-Si samples passivated by a 10 nm thick Al_2O_3 layer only (black) and after the deposition of a 100 nm thick a-SiN_x:H layer and co-firing at 860 ˚C peak temperature (red) as a function of the annealing temperature. Figure 26 (a) shows the effective minority carrier lifetime in *c*-Si samples with hydrophobic surfaces prior to Al_2O_3 deposition and (b) hydrophilic *c*-Si surfaces.

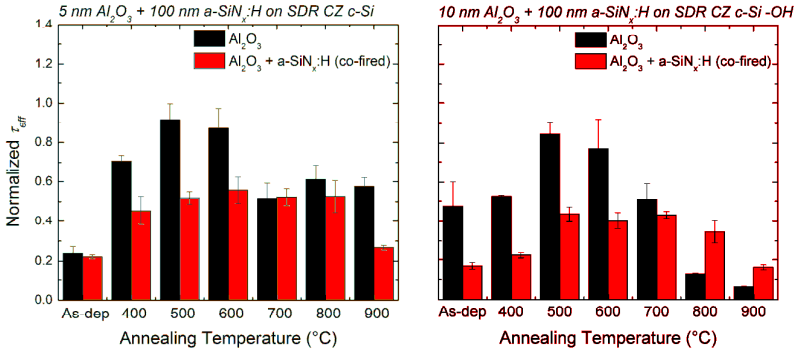

Figure 26: Effective minority carrier lifetime at $\Delta n = 1\times10^{15}$ cm^{-3} in *c*-Si samples with (a) hydrophobic and (b) hydrophilic surfaces passivated by a 10 nm thick Al_2O_3 layer only (black) and after a-SiN_x:H capping and co-firing (860 ˚C, peak temperature) (red). After Al_2O_3 deposition, the samples are annealed for 20 minutes in N_2 environment at the indicated temperature. τ_{eff} is shown as a function of the annealing temperature prior to a-SiN_x:H deposition. All lifetimes have been normalized to the highest value (113 µs).

In case of passivation by an Al_2O_3 layer only, both Figure 26 (a) and (b) shows that the same trend; the effective minority carrier lifetime increases after a low (< 800 ˚C) thermal treatment thanks to the formation of fixed negative charges. Effective minority carrier lifetimes decrease after a high (≥ 800 ˚C) temperature anneal, caused by an increased interface defect density (see Section 3.1.1). Effective minority carrier lifetimes in *c*-Si substrates with hydrophobic surface are slightly higher than lifetimes in *c*-Si samples with hydrophilic surfaces due to the lower interface defect density. For both surface finishes, effective minority carrier lifetimes in *c*-Si passivated by stacks with an Al_2O_3 annealed at low (≤ 700 ˚C) temperature decreased after co-firing. Hydrogen is released from the Al_2O_3/a-SiN_x:H interface, resulting in an increase of the interface defect density. Lifetimes in c-Si samples with hydrophilic surface finishing, annealed at ≤ 800 ˚C are significantly lower compared to lifetimes in equivalent samples with hydrophobic

surface finishing. It has been hypothesized that the effective minority carrier lifetime is reduced by residuals of the wet-chemical cleaning which induce a reduction of the lifetime after an high temperature thermal treatment. However, more insight is needed to confirm this hypothesis .
After a-SiN_x:H capping and co-firing, the highest lifetime is observed samples passivated by a stack with an Al_2O_3 layer annealed at 600 (hydrophobic) and 700 ˚C (hydrophilic) prior a-SiN_x:H capping. At lower (< 600 ˚C) annealing temperature, the level of surface passivation is decreased by blister formation, and at high (≥ 800 ˚C) annealing temperature are lifetimes reduced by an increased surface defect density. Anneal the samples at 600 ˚C is the best trade-off between on one hand, outgassing of fragment to prevent blister formation during co-firing, and on the other hand, maintaining the low surface defect density. Lifetimes in *c*-Si samples with hydrophilic is lower compared to the hydrophobic surface fishing. As hypothesized above, residuals of the wet-chemical clean used for preparation of the hydrophilic surface finishing reduce the effective minority carrier lifetime after a high temperature treatment.

Conclusion
In this Section, the influence of the thermal treatments on the *c*-Si surface passivation quality of the Al_2O_3/*c*-SiN_x:H stack has been investigated. It has been shown that blisters are formed in the Al_2O_3/a-SiN_x:H passivation stack during co-firing. The film stress and capping effect of the stack is enhanced compared to Al_2O_3 layers. Therefore, effusion of gaseous species and increased film stress result in partial de-lamination of the passivation stack. The blistered area decreases as a function of the annealing temperature due to the temperature dependency of the effusion of species. Blister-free passivation stacks can be manufactured by annealing thin (≤ 10 nm) Al_2O_3 prior to the deposition of the a-SiN_x:H layer. Less H_2O, H_2 and CO_2 is released during the final co-firing step due to outgassing of the layer prior to a-SiN_x:H deposition.
Furthermore, it has been shows that the passivation quality improves after an low (≤ 700 ˚C) temperature anneal thanks to the formation of fixed negative charges. Annealing the passivation layers at high (> 700 ˚C) temperature leads to an increase of the interface defect density consequently followed by a decrease of the effective minority carrier lifetime.
After co-firing, lifetimes decrease due to an increase of the interface defect density and blistering formation. The highest effective minority carrier lifetime has been reported in *c*-Si samples with hydrophobic surfaces, passivated by 10 nm thick Al_2O_3 layers annealed at 600 ˚C prior to deposition of the a-SiN_x:H layer. Annealing the samples at 600 ˚C is the best tradeoff between one hand, outgassing of species to prevent blistering formation and on the other hand maintaining the low surface defect state density.

3.3.Solar cell results

Introduction
In Section 3.2, *c*-Si surfaces successfully have been passivated by Al_2O_3/a-SiN_x:H stacks. Al_2O_3 films reduce the surface defect density (D_{it}) and the negative fixed charges within the passivation layers repel minority carriers from surface defects leading to improved effective minority carrier

lifetimes. It has been suggested that the use of Al_2O_3 films as rear surface passivation layer in *p*-type Si solar cells will lead to an improvement of the open circuit voltage (V_{oc}) due to the passivation of dangling bonds [13]. The improvement of the V_{oc} will lead to higher conversion efficiencies compared to PERC solar cells with thermal grown SiO_x rear passivation layers. In this Section, *p*-type *c*-Si solar cells passivated by Al_2O_3/a-SiN_x:H rear passivation stacks are manufactured, characterized and compared to the performance of standard *i*-PERC cells. Furthermore, blistered passivation stacks will be used to design an alternative solar cell production process.

3.3.1. Local Al BSF outgassed Al_2O_3 passivated *c*-Si solar cells

As demonstrated in Section 3.2, blister formation should be avoided for the highest level of surface passivation. Another disadvantage of blisters in the passivation layer is that local BSF can be formed trough blister openings. The formation of the local BSF through blister openings is displayed in Figure 27. Figure 27 (a) shows the rear of an Al_2O_3 passivated local BSF *c*-Si solar cell after co-firing. Figure 27 (b) displays a SEM cross-section of a local BSF formed trough a blister opening. The Figure clearly displays the formation semiconductor-metal contact through the blisters in the passivation stack.

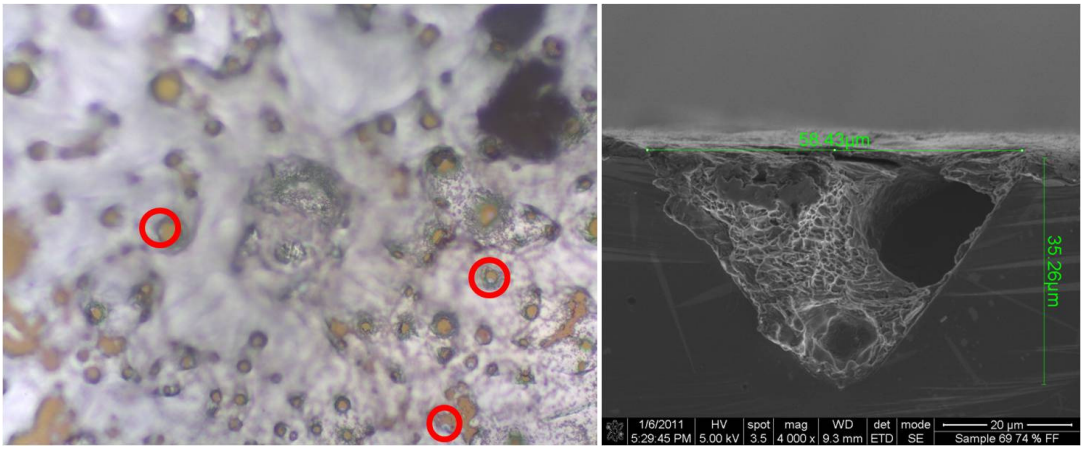

Figure 27: (a) Optical microscope picture (400 x) of the back of the Al_2O_3 passivated local BSF Si solar cell after co-firing. The red circles indicate blistering of the passivation stack. (b) Cross-section SEM image of a local Al BSF formed through a blister opening. The triangle shaped region is a p^{++} local back surface field formed during the co-firing.

The formation of local BSF through reduces the V_{oc} and therefore the conversion efficiency significantly. This can be understood by using the ideal one diode equation to give an expression for the open circuit voltage (V_{oc}) [13]:

$$V_{OC} = \frac{kT}{q} \ln\left(\frac{J_{SC}}{J_{oe} + J_{ob}} + 1\right) \qquad (12)$$

With J_{oe} and J_{ob} the emitter saturation current density and the base saturation current density respectively. The emitter saturation current can be extracted from symmetrical device structures using QSSPC measurements [15]. J_{ob} can be approximated by [13]:

$$J_{ob} = \frac{qDn_i^2}{L_{eff} N_A} \tag{13}$$

Where q is the elementary charge, D the diffusion coefficient of minority carriers in the base, N_A the acceptor density, n_i the intrinsic carrier concentration and L_{eff} the effective diffusion length. The last value can be described by Equation (14) [47].

$$L_{eff} = L_{bulk} \times \frac{1 + \frac{S_{eff,rear} \times L_{bulk}}{D} \tanh\left(\frac{W}{L_{bulk}}\right)}{\frac{S_{eff,rear} \times L_{bulk}}{D} + \tanh\left(\frac{W}{L_{bulk}}\right)} \tag{14}$$

In Equation 18, L_{bulk} is the bulk diffusion length, W the substrate thickness and $S_{eff,rear}$ the effective rear surface recombination velocity. $S_{eff,rear}$ can be described by the following relation [46]:

$$S_{eff,rear} = S_{eff,pass}\left[1 - (X + YZ)\right] + S_{eff,metal}(X + YZ) \tag{15}$$

In Equation (15), X is the metalized fraction, typically 0.0147 in a standard *i*-PERC cell [46], Y the blistering fraction (see Figure 24), Z the fraction of blisters trough which local BSF are formed during co-firing (estimated to be 0.4), $S_{eff,metal}$ the effective surface recombination velocity of the metalized area, calculated to be 1726 ± 74 cm s^{-1} and $S_{eff,pass}$ the effective surface recombination velocity of the passivation area [46]. Equation (15) is valid if under the assumption that non-contacted blisters have an equal level of surface passivation as non-blisters areas. An approximation of the effective surface recombination velocity of the passivated area is displayed by Equation (2) [13]. Where the effective minority carrier lifetime can be determined by QSSPC measurements and τ_{bulk} the bulk lifetime, calculated to be 690 µs at $\Delta n = 1\times10^{15}$ cm^{-3}. Using the data from Section 3.2 and Equation (2), one can calculate that $S_{eff,pass}$ is in the range from 50 to 200 $cm\cdot s^{-2}$.

Using Equation (15), one can see that the effective surface recombination is affected significantly by the formation of blisters; $S_{eff,metal}$ is significant higher compared to $S_{eff,pass}$, and therefore, a larger contact area results to an increase of the effective rear surface recombination velocity. As shown by Equation (12) – (15) depends the V_{oc} on $S_{eff,rear}$, therefore, reduction $S_{eff,rear}$ is consequently followed by a reduction of the V_{oc}.

As demonstrated in Section 3.2 and in the Section above, blistering should be avoided for optimal use of the passivation layer. Blistering is partial de-lamination of a passivation film or

stack caused on one hand desorption of gaseous species from the Al_2O_3 layer or the *c*-Si substrate and on the other hand the increased film stress upon thermal treatment. The capping effect and the film stress depends on the film thickness, therefore, it has been shown that blister-free passivation stacks can be formed by outgassing thin (5-10 nm) Al_2O_3 prior to deposition of the a-SiN_x:H layer. The highest level of *c*-Si surface passivation has been provided by 10 nm thick Al_2O_3 layers annealed at 600 ˚C prior to deposition of the a-SiN_x:H layer (Section 3.2.3).

c-Si solar cells are produced from 12.5 x 12.5 cm^2 semi-square 2 ± 1 Ω·cm CZ *p*-type *c*-Si wafers with a thickness of 150 ± 10 µm with an emitter of 60 $\Omega \cdot sqr^{-1}$, using the production process as displayed in Section 2.1. The hydrophobic *c*-Si surface state is used prior to the deposition of the rear passivation layer. The thermally grown high quality SiO_x rear passivation layers, deposited at step 6, are replaced by 10 nm thick Al_2O_3 passivation layers. 10 nm thick Al_2O_3 layers provide the highest level of surface passivation as shown in Section 3.2. After the deposition of the Al_2O_3 layers, the substrates received a thermal anneal in N_2 environment for 20 minutes at a temperature varying from 200 to 700 ˚C, prior to a-SiN_x:H deposition, in order minimize the outgassing of gaseous species during the final co-firing step. Standard *i*-PERC solar cells are produced as reference by the process as described in Section 2.1. Current-voltage (I-V) curves of both cell types were measured by a steady-state Xe lamp solar simulator (Wacom Electrics Co., WXS-200S-20, 1 sun). The average and the best cell results with respect to conversion efficiency (η), Fill Factor (*FF*), open circuit voltage (V_{oc}) and short circuit current (J_{sc}) of the *c*-Si solar cell with Al_2O_3 rear passivation and the *i*-PERC solar cell are displayed in Table 9. Furthermore, Figure 28 displays the open circuit voltage as a function of the Al_2O_3 annealing temperature.

Table 9: Overview of the cell characterization results (1 sun) for the 148.25 cm^2 *i*-PERC and local Al BSF *c*-Si solar cells with Al_2O_3 passivated rear. The cells are 150 µm thick, have a base resistivity of 2 Ω·cm and an emitter of 60 $\Omega \cdot sqr^{-1}$

Cell type		Size (cm^2)	J_{sc} (mA cm^{-2})	V_{oc} (mV)	FF (%)	Eta (%)
***i*-PERC Reference**	Average of 4 cells	148.25	37.1 ± 0.1	636.1 ± 1.2	77.7 ± 0.6	**18.4 ± 0.2**
	Best cell	*148.25*	*37.1*	*636.8*	*78.2*	***18.5***
Best Al_2O_3 pass. Local Al BSF Cell	Average of 4 cells	148.25	36.7 ± 0.3	641.2 ± 0.2	77.3 ± 0.7	**18.2 ± 0.1**
	Best cell	*148.25*	*36.6*	*641.1*	*77.7*	***18.2***
Absolute gain			***-0.4***	***+ 5.1***	***-0.4***	***-0.2***

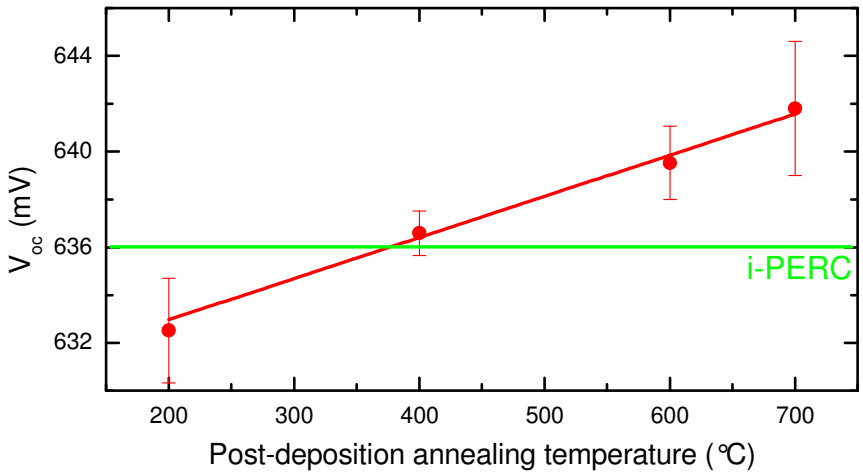

Figure 28: Average V_{oc} of local Al BSF *c*-Si solar cells with Al_2O_3 passivated rear as a function of the post-deposition annealing temperature (for 20 minutes in N_2 environment) prior to a-SiN_x:H deposition. The green line displays the average V_{oc} of *i*-PERC reference cells.

In case of local Al BSF *c*-Si solar cells with Al_2O_3 passivated rear, a maximum average conversion efficiency of 18.2 % is reported for the best conditions (10 nm thick Al_2O_3 outgassed at 700 ˚C for 20 minutes in N_2 environment). The *i*-PERC reference cells show an average η of 18.4 %. Table 9 displays an average gain in V_{oc} of 5.1 mV, however, J_{sc} decreased by -0.4 mA cm^{-2} with respect to the *i*-PERC reference cell. Slightly lower fill factors (-0.4 %) are reported in case of local Al BSF solar cells with Al_2O_3 rear passivation. Figure 28 clearly shows that V_{oc} improves as a function of the outgassing temperature.

Table 9 and Figure 28 depict that the use of Al_2O_3 as passivation layer leads to an improvement of the V_{oc}. Figure 28 shows the V_{oc} improves as a function of the annealing temperature. Blistering occurs in the stack with Al_2O_3 annealed at low anneal temperatures (≤ 400 ˚C), as reported in section 3.1.7. This blistering formation lowers the effective minority carrier lifetime, and local BSF can be formed through the blister openings, resulting in a decreased V_{oc}. As demonstrated in Section 3.1.7, the blistered area decreases as a function of the annealing temperature due to the effusion of species. No significant decrease of fixed negative charged or increase of surface defect density is observed (see section 3.1.1) proving that V_{oc} improvements are the result of a decreased blistered area. The optimum annealing temperature is slightly higher than reported in Section 3.2. Apparently, the V_{oc} is more affected by the formation of blister that by an increase of the surface defect density.

Figure 28 shows that using Al_2O_3 films as surface passivation the V_{oc} improves. Nevertheless, J_{sc} decreases by 0.4 mA cm^{-2} due to a reduction of the back reflectance. Reflectance measurements from 1000 to 1200 nm show a decreased reflectance of Al_2O_3/a-SiN_x:H (10 nm/100 nm thick) stacks compared to the reflectance of SiO_x/a-SiN_x:H (10 nm/100nm thick) stacks [46]. Lower J_{sc} together with decreased fill factors leads to a reduction of the conversion efficiency by 0.2 %

with respect to *i*-PERC reference cells. However, optimization of the back reflectance (using a thick (> 250 nm) SiO_2 reflection layer) will lead to higher J_{sc} and therefore higher efficiencies. We expect that local Al BSF *c*-Si solar cells with Al_2O_3 passivated rear will have higher conversion efficiencies than *i*-PERC reference cells, if the cells are passivated by an optimized rear passivation stack with respect to the back reflectance (increased J_{sc}) and using optimized (blister-free). Al_2O_3 layers *p*-type CZ *c*-Si solar cells with an average conversion efficiency of 19.0 % have been constructed using Al_2O_3/SiO_2/a-SiN_x:H rear passivation stack [13].

3.3.2. Random Al BSF Al_2O_3 passivated *p*-type *c*-Si solar cells

The level of passivation, and hereby the open circuit voltage, is affected significantly by the surface coverage area of the passivation layer, as described above, leading to the conclusion that solar cell efficiency is reduced by the formation of blisters in the passivation stack. However, this Section will show that blisters can be used to design alternative solar cell production sequences [48]. At present, PERC point contact formation is industrially viable in two ways [49]: (a) the *i*-PERC process, where the dielectric is opened via laser ablation of the passivating dielectric before the rear-side metallization, and (b) laser-fired contracts (LFC), where the contacts are laser-fused after metallization. In this Section, blistering is proposed as an approach to create semiconductor-meal contacts. Using the blister openings, solar cells can be produced without laser opening. Using blisters for the formation of BSF also proves that the V_{oc} is affected by the formation of semiconductor-metal contacts through the blister openings in PERC cells.

It has been proven in Section 3.1.7, that the blister density is influenced by the film thickness and thermal treatment. 12.5 x 12.5 cm^2 semi-square random, random Al BSF CZ *p*-type *c*-Si solar cells are made, using the production sequence as described in Table 10. Semiconductor-metal contacts are formed through the randomly distributed blister openings in the rear passivation stack. As rear surface passivation for the random, stacks of Al_2O_3 and a-SiN_x:H are used. As well hydrophilic and hydrophobic pre-ALD cleanings and Al_2O_3 films of 5, 10 and 30 have been used. The alumina layers are annealed for 20 minutes at 350 ˚C prior to deposition a-SiN_x:H layer for the formation of the fixed negative charges in the passivation layer. Full Al BSF c-Si solar cells are produced as reference using the baseline as displayed in Table 10 and Section 2.1. The cells are measured by a steady-state Xe lamp solar simulator (Wacom Electrics Co., WXS-200S-20, standard conditions, AM 1.5G). The cell characteristics of the random Al BSF solar cells and the full Al BSF are depicted in Table 11. The average size and density are measured before and after the co-firing step, and displayed in Figure 29 (a). The average J_{sc}, V_{oc} and *FF* and conversion efficiency values of local Al BSF cells fired at 860 ˚C are shown Figure 29 (b) and (c).

Table 10: Baseline of random Al BSF (left), full Al BSF reference (right) *p*-type *c*-Si solar cell process sequences. The 148.25 cm^2 cells are 150 µm thick, have a base resistivity of 2 Ω·cm and an emitter of 60 Ω·sqr^{-1}

Al_2O_3 pass. P-type Si solar cells	Full Al BSF P-type Si solar cells
Texturing front and polish rear	
Diffusion ($POCl_3$) front	
Pass. rear (Al_2O_3 + SiN_x:H)	
Anti-reflection coating (a-SiN_x:H) front	
Laser ablation rear	
Al sputtering or screen-printing rear	
Ag screen-printing front	
Co-firing	

Table 11: Overview of the cell characterization results (AM 1.5G) for the random local AL BSF solar cell and the full Al BSF reference cell.

Cell type		Size (cm^2)	J_{sc} (mA cm^{-2})	V_{oc} (mV)	FF (%)	Eta (%)
Full Al BSF reference	Average of 4 cells	148.25	35.6 ± 0.1	622.0 ± 1.5	75.1 ± 0.6	**16.6 ± 0.2**
	Best cell	*148.25*	*35.7*	*623.5*	*75.7*	***16.8***
Random local Al BSF cells	Average of 4 cells	148.25	36.9 ± 0.0	627.0 ± 1.6	75.1 ± 0.7	**17.4 ± 0.1**
	Best cell	*148.25*	*36.9*	*626.1*	*75.8*	***17.5***
Absolute gain			**+ 1.3**	**+ 5.0**	**+ 0.0**	**+ 0.8**

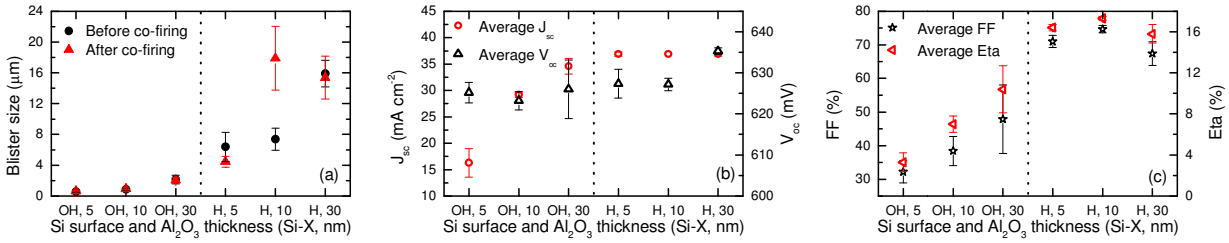

Figure 29: (a) The average blister size before and after co-firing, (b) average J_{sc} and average V_{oc} and (c) average *FF* and average η of random Al BSF *c*-Si Solar cells with pre-deposition clean and Al_2O_3 thickness displayed on the x-axis. All the cells have been co-fired at 860 ˚C peak temperature.

Figure 29 shows that for the best cells, the average V_{oc} and J_{sc} of random local Al BSF cell improve compared to the full Al BSF reference cell. No significant difference in fill factor is observed, however, the improved J_{sc} and V_{oc} leads to an absolute average conversion efficiency gain of + 0.8 %.

One can see in Figure 29 (a) that small blisters (≤ 2 µm) are formed in stacks with Al_2O_3 deposited on hydrophilic *c*-Si surfaces and large (≥ 5 µm) blisters are formed in case of Al_2O_3

deposited on *c*-Si with hydrophobic surface finishing. Figure 29 (b) shows an improvement of V_{oc} as a function of the film thickness. Furthermore, Figure 29 (b) shows the increase of J_{sc} as a function of the layer thickness. The improved V_{oc} and J_{sc} leads to an improvement of the fill factor and the conversion efficiency, as depicted in Figure 29 (c).

From Figure 29, it is obvious that a minimum blistering size in needed to enable contacting. The highest *FF* and J_{sc} are observed in solar cells passivated by 10 nm thick Al_2O_3 layers deposited on hydrophobic *c*-Si surfaces. According to Figure 24, 7 % of the passivation stack is de-laminated after the final co-firing step. The hydrophilic surface finishing is less favorable since the blisters are too small to form semiconductor-metal contact, consequently resulting in a decrease of J_{sc}, V_{oc} and *FF*. From Figure 29, one can learn that the solar cell performance is affected significantly by (pre-/post-) deposition conditions and that optimum production process is very narrow.
Using 10 nm thick Al_2O_3 layers deposited on hydrophobic *c*-Si surfaces as rear passivation layer of solar cell leads to an average cell conversion efficiency of 17.4 %, as displayed in Table 11. There is an apparent gain in J_{sc} and V_{oc} of 1.3 mA cm^{-2} and 5 mV respectively, because of an improved internal reflection and rear surface passivation compared to the full Al BSF cell.

Conclusion

In this Section, surfaces of *c*-Si solar cells have been passivated successfully by Al_2O_3 thin films. The average V_{oc} of solar cells with an optimized rear passivation stack increased by 0.4 % compared to the average V_{oc} of *i*-PERC solar cells. It has been proven that the formation of blister during the final co-firing step results in a reduction of the V_{oc}. Blister-free Al_2O_3 rear passivated *c*-Si solar cells were manufactured by using 10 nm thick Al_2O_3 films and annealing these films at 700 ˚C temperature prior to a-SiN_x:H. The conversion efficiency was not higher than the conversion efficiency of a standard *i*-PERC solar cell, due an decreased J_{sc}. The J_{sc} is reduced due to a reduction of the internal reflection. It has been expected that optimization of the rear stack with respect to the reflectivity will lead to higher conversion efficiencies.
Furthermore, *c*-Si solar cells were produced using the blister openings in the rear passivation stack. Random local back surface fields were formed through the blister openings.

4. Conclusion

This study gives an overview of the effect of a thermal treatment on the material and layer properties of ALD Al_2O_3 thin films. The effect has been investigated in order to optimize the passivation quality of Al_2O_3/a-SiN_x:H stacks. These stacks are used as rear passivation stack in *c*-Si solar cells. It has been shown that on lifetime level, the highest level of *p*-type *c*-Si surface passivation is provided by stacks with 10 nm thick Al_2O_3 films, annealed at 600 ˚C in N_2 environment for 20 minutes, prior to the deposition of the a-SiN_x:H layer.

It has been reported that as-deposited Al_2O_3 layers are amorphous, have a positive fixed charge density of $(0.8 \pm 0.5) \times 10^{11}$ cm^{-2} and have a hydrogen concentration of 2.0 at.%. The interface defect density is higher in the case that Al_2O_3 is deposited on hydrophilic *c*-Si surface compared to the case the Al_2O_3 is deposited on hydrophilic c-Si surfaces. This is due to the low quality SiO_x interfacial layer, present between Al_2O_3 films and hydrophilic *c*-Si surfaces.

It has been proven that a post-deposition thermal anneal is required to form fixed negative charges. H_2O, H_2 and CO_2 effuse from Al_2O_3 layer and a SiO_x interfacial layer is formed or enhanced during a thermal treatment. The SiO_x interfacial thickness increases as a function of the annealing temperature. After a thermal anneal, material and layer characteristics are not influenced by the *c*-Si surface finishing. The interface defect density increases after a high temperature ($\geq$ 800 ˚C) treatment due to the depletion of H from the Al_2O_3/*c*-Si interface. 30 nm thick amorphous Al_2O_3 layers transform into γ-Al_2O_3 during a high temperature treatment. Blisters are formed in thick ($\geq$ 30 nm) Al_2O_3 layers due to the capping effect of the dielectric film and the increased film stress. The capping effect of the layer prevents the effusion of species this causes delamination of the film.

Al_2O_3/a-SiN_x:H stacks are affected by blister formation even more. The a-SiN_x:H layer enhances the capping effect and the film stress depends linearly on the stack thickness. It has been proven that blister formation in Al_2O_3/a-SiN_x:H stacks should be avoided in order to optimize their passivation quality. On one hand, blisters remove fixed negative charges from the *c*-Si surface, and on the other hand, local aluminum back surface fields can be formed through blister openings. Both phenomena reduce the effective minority carrier lifetime in *c*-Si solar cells and thereby the conversion efficiency. Furthermore, it has been shown that the passivation quality of Al_2O_3/a-SiN_x:H stacks decreases during co-firing due to blister formation and depletion of H from the Al_2O_3/a-SiN_x:H interface.

Blister formation in Al_2O_3/a-SiN_x:H stacks can be prevented by using thin (5-10 nm thick) Al_2O_3 layers and outgassing these layers prior to the deposition of the a-SiN_x:H layer. Thin Al_2O_3 are favorable due to the fact that the film stress, the effusion of H_2O, H_2 and CO_2 from the material and the capping effect depend on the film thickness. The highest level of *c*-Si surface passivation has been provided by Al_2O_3/a-SiN_x:H stacks, with thin Al_2O_3 films outgassed at 600 ˚C prior to a-SiN_x:H deposition. Annealing the samples at 600 ˚C is the best tradeoff between on one hand, outgassing of species to prevent blister formation and on the other hand maintaining the low

interface defect density. The highest effective minority carrier lifetime has been reported in *c*-Si samples with the hydrophobic surface finishing prior to Al_2O_3 deposition.

Optimized Al_2O_3/a-SiN_x:H stacks have been integrated successfully into *p*-type CZ *c*-Si solar cells: the average V_{oc} increases due to the Al_2O_3/a-SiN_x:H rear passivation stacks. It has been shown that the V_{oc} increases linearly with the annealing temperature due to the reduction of the blistered area. The best cell results were obtained using Al_2O_3/a-SiN_x:H rear passivation stacks with thin ($\leq$ 10 nm) Al_2O_3 films, annealed at 700 ˚C for 20 minutes in N_2 environment, prior to the deposition of the a-SiN_x:H capping layers. The average V_{oc} increases with 5.1 mV compared to the average V_{oc} of *i*-PERC *c*-Si solar cells.

Furthermore, it has been proven that the blistering formation can be used to design a *c*-Si solar cell production sequence without opening the passivation stack intentionally by laser ablation. Random local aluminum back surface fields can be induced through the blisters.

5. Outlook

In this study, thermal ALD grown (using TMA + H_2O) Al_2O_3 thin films have been successfully integrated as rear passivation layer in *p*-type CZ *c*-Si solar cells. The average V_{oc} increases due to the use of Al_2O_3/a-SiN_x:H rear passivation stacks. Furthermore, it has been demonstrated that the solar cell performance is influenced by blister formation in the passivation stack. It has been hypothesized that desorption of gaseous species together with an increased film stress leads to the formation of these blisters upon a thermal treatment; the capping effect of the passivation stack prevents the outgassing of H_2O, H_2 and CO_2, causing delamination of the film. Using thin (5-10 nm thick) films and outgassing these layers prior to a-SiN_x:H deposition prevents formation of blisters upon co-firing. Therefore, the highest V_{oc} has been reported when the *c*-Si surfaces were passivated by 10 nm thick Al_2O_3 films annealed at 700 ˚C for 20 minutes in N_2 environment prior to a-SiN_x:H deposition.

This study gives an overview of phenomena that occur during a thermal treatment; however, not all the mechanisms (e.g. SiO_x interface and fixed negative charge formation, difference in blister size between hydrophobic and hydrophilic surface finishing) have been investigated in detail yet. These insights can possibly be used to optimize the passivation quality and the c-Si solar cell production process even more.

Al_2O_3/a-SiN_x:H stacks has been optimized to passivated CZ *c*-Si surfaces. It has been shown that the highest level of surface passivation is provided by 5-10 nm thick Al_2O_3 layers annealed at 600 ˚C. However, passivation layer characteristics and post-deposition thermal treatment required for optimal passivation of FZ *c*-Si surfaces can differ significantly from the layers and the thermal treatments used in this work. The passivation stacks in this work have been optimized specifically for CZ *c*-Si substrates.

Both blister formation and the level of passivation have been investigated by varying the annealing temperature while keeping the annealing time and environment fixed. Using this method, it has been proven that the blistered area decreased as a function of the annealing temperature. The effect of the annealing time on the blistering formation in the passivation stack has not been investigated. Possibly, blister-free passivation stacks can be obtained by applying another thermal budget (e.g. longer annealing time, lower annealing temperature).

It has been observed that the interface defect density increases significantly after a thermal anneal at high temperature (≥ 800 ˚C). The increase of the interface defect density is caused by the depletion of hydrogen from the *c*-Si interface. Annealing the samples in a forming gas (H_2) environment (especially during the cooling down) can lead to maintaining the low level of interface states. The effect of a forming gas environment has not been investigated in this study.

Blistering has been investigated for the case of Al_2O_3 deposited by a temporal ALD process using TMA and H_2O. Al_2O_3 films can also be manufactured using TMA and O_3 or TMA and an oxygen plasma (plasma-enhanced ALD). Blistering has also been observed in layers deposited by other deposition processes; however, it is likely that the blistering conditions differ from those observed in this study, since the level of contamination, and therefore the outgassing, is

influenced by the deposition method [25,28]. It is even likely that blistering conditions are different in Al_2O_3 films deposited using a spatial ALD deposition process with TMA and H_2O. One should investigate blistering conditions for every deposition method for optimal use of the Al_2O_3 films as *c*-Si passivation layer.

As demonstrated in Section 3.2, the passivation quality is influenced by the *c*-Si surface state prior to the deposition of the Al_2O_3. Especially high (> 700 ˚C) temperature thermal treatments reduce the effective carrier lifetime significantly. The drastically decrease of lifetime was attributed to the presence of residuals of the ammonia-peroxide-mixture cleaning step; however, this hypothesis has not been investigated. More insight is needed to confirm this hypothesis.

This study focuses on the effective minority carrier lifetime in *c*-Si in order to optimize the solar cell efficiency. However, optical properties (e.g. refractive index) influence the solar cell performance significantly (as demonstrated in Section 3.3). More insight in the optimal properties of the stack is required to determine the influence of the optical properties of the stack on the performance of the *c*-Si solar cell.

Acknowledgement

I would like to express my gratitude to all those who gave me the possibility to complete this work. First of all, I would like to thank IMEC for giving me the opportunity to complete my master thesis by making me a member of the PV platform group. Furthermore, I would like to thank IMEC for giving me the freedom to combine my study with my volleyball activities. Especially, I would like to thank my daily supervisor Bart Vermang for his grateful help. His knowledge, creativity and hard-working mentality always inspired me and helped me to finish this work. He always challenged me and was always willing to help me despite the fact that I was 'de Hollander' no matter how hard I tried to integrate. I would also like to thank Joachim John for keeping the overview and for correcting my work. Furthermore, I would like to thank Alessandro Morato, Ingrid de Wolf and Shuji Tanaka for their help with C-V, stress and TDS measurements respectively.

I also want to acknowledge my supervisor for University of Technology, Prof. Erwin Kessels for the fruitful discussions, detailed corrections and for keeping me on track. He was always able to provide me the necessary knowledge and he always added some useful remarks thanks to the fact that he is one of the first who proved the advantages of the use of Al_2O_3 films in *c*-Si solar cells.

I would also like to thank my volleyball club, first Schuvoc Halen, afterward Aquacare Halen en now Soleco Herk-de-Stad. Thanks to their flexibility and their understanding I was able to finish my study and play volleyball at the highest level in Belgium, which I have enjoyed since the first day.

Finally, I would gratefully thank my family and friends. Especially, I would like to thank my parents. They always give me the possibility to develop myself, and supported me emotionally and financially. Mam, ik hoop dat je trots bent. Furthermore, I would gratefully like to thank my girlfriend Inge for her love, support and faith, despite the tough time. I significantly improved my presentation skills thanks to her communication talent.

Bibliography

[1] Sustainable Energy systems. [Online] http://www.wbgu.de.

[2] *Memoire sur les effets electriques produits sous l'influence des rayons solaires.* **E. Becquerel.** 1839, Comptes Rendus, Vol. 9, pp. 561-567.

[3] *A New Silicon p-n junction photocell for converting solar radiation into electrical power.* **D.M. Chapin, C.S. Fuller, G.L. Pearson.** Journal of Applied Physics, 1954, Vol. 25, pp. 1721-711.

[4] *24.5 % Efficiency silicon PERT Cells on MCZ substrates and 24.7% efficiency PERL cells on FZ substrates.* **J. Zhao, A. Wang, M.A. Green.** 1999, Progress in Photovoltaics: Research and Applications, Vol. 7, pp. 471-474.

[5] *Solar cell efficiency tables (version 37).* **M.A. Green, K. Emery, Y. Hishikawa, W. Warta.** 2011, Progress in Photovoltaics: Research and Applications, Vol. 19, pp. 84-92.

[6] **EPIA.** European Photovoltaic Industry association (EPIA). [Online] http://www.epia.org/.

[7] **Internation Energy Agency.** Technology roadmap solar photovoltaic energy. [Online] E, 2010. http://www.iea.org/papers/2010/pv_roadmap.pdf.

[8] **B. Hoex.** *Functional thin film for high-efficiency solar cells.* Einhoven, TU/e : proefschrift, 2008.

[9] *Very low surface recombination velocities on p-type silicon wafers passvivated with a dielectric with fixed negavie charge.* **G.Agostinelli, A. Delabie, P. Vitanov, Z. Alexieva, H.F.W. Dekkers, S. de Wolf, G.Beaucarne.** 2006, Solar Energy Materials & Solar cells, Vol. 90, pp. 3438-3443.

[10] *Ultralow surface recombination of c-Si substrates passivated by plams-assisted atomic layer deposition of Al_2O_3.* **B. Hoex, S.B.S. Heil, E. Langereis, M.C.M. van de Sanden, W.M.M. Kessels.** 2006, Applied Physics Letters, Vol. 89, p. 04112.

[11] *Stability of Al_2O_3 and Al_2O_3/a-SiN_x:H stacks for surface passivation of crytalline silicon.* **G. Dingemans, P. Engelhart, R. Seguin, F. Einsele, B. Hoex, M.C.M. van de Sanden, W.M.M. Kessels.** 2009, Journal of Applied Phyisics, Vol. 106, p. 114907.

[12] **E. Cornagliotti.** *Advanced Characterization of Novel Solar Grade Materials for Solar Cells.* Leuven : KUL, proefschrift, 2011.

[13] *Approach for Al_2O_3 rear surface passivation of industrial p-type Si PERC above 19 %.* **B. Vermang, H. Goverde, L. Tous, A. Lorenz, P. Choulat, J. Horzel, J. John, J. Poortmans, R. Mertens.** 1002, 2012, Progress in Photovoltaics, Vol. 10, p. 2196.

[14] *Statistics of the recombination of holes and electrons.* **W. Shockley, W.T. Read.** 5, Physical Review letters, Vol. 87, pp. 835-842.

[15] *Contactless determination of current-voltage characteristics and minority-carrier lifetimes in semiconductors from quasi-steady-state photoconductance data.* **R.A. Sinton, A. Cuevas.** 7, 1996, Applied Physics Letters, Vol. 69, p. 117723.

[16] *On the c-Si passivation mechanism by the negative-charge-dielectric Al2O3.* **B. Hoex, J.J.H. Gielis, M.C.M. van de Sanden, W.M.M. Kessels.** 2008, Journal of Applied Physics, Vol. 104, p. 113703.

[17] *Effective passivation of Si surfacers by plasma deposited SiO(x)/a-SiN(x):H stacks.* **G. Dingemans, M.M. Mandoc, S. Bordihn, M.C.M. van de Sanden, W.M.M. Kessels.** 22, 2011, Applied physics letters, Vol. 98, p. 222102.

[18] *Silicon surface passivation by atomic layer deposited Al_2O_3.* **B. Hoex, J. Schmidt, P. Pohl, M.C.M. van de Sanden, W.M.M. Kessels.** 2008, Journal of Applied Physics, Vol. 104, p. 044903.

[19] *Influence of the oxidant on the chemical and field-effect passivation of Si by ALD Al_2O_3.* **G. Dingemans, N.M. Terlinden, D. Pierreux, H.B. Profijt, M.C.M. van de Sanden, W.M.M. Kessels.** 1, 2011, Electrochemical and Solid-State Letters, Vol. 14, pp. H1-H4.

[20] *Compositional and structural analysis of aluminum oxide films prepared by plama-enhanced chemical vapor deposition.* **Y.-C. Kim, H.-H. Park, J.S. Chun, W.-J. Lee.** 1994, Thin Solid Films, Vol. 237, pp. 57-65.

[21] **D.K. Schroder.** *Semiconductor material and device characterization.* 2nd edition. New York : John Wiley & Sons inc., 1998.

[22] *Hydrogen effusion: a probe for surface desoption and diffusion.* **W. Beyer.** 1991, Physica B, Vol. 170, pp. 105-114.

[23] *Electrical characterization of thin Al_2O_3 films grown by atomic layer deposition on silicon and various metal substrates.* **M.D. Groner, J.W. Elam, F.H. Fabreguette, S.M. George.** 2002, Thin Solid Films, Vol. 413, pp. 186-197.

[24] *Quantitative analysis of the effect of disorde-induced mode coupling on infrared absorption in silica.* **C.T. Kirk.** 2, July 15, 1988, Physical Review B, Vol. 38, pp. 1255-1273.

[25] *Composition and bonding structure of plasma-assisted ALD Al_2O_3 films.* **V. Verlaan, L.R.J.G. van den Elzen, G. Dingemans, M.C.M. van de Sanden, W.M.M. Kessels.** 3-4, 2010, Physica Status Solidi C, Vol. 7, pp. 976-979.

[26] *Gas diffusion barriers on polymers using multilayers fabricated by Al_2O_3 and rapid SiO2 atomic layer deposited.* **A.A Dameron, S.D. Davidson, B.B. Burton, P.F Carcia, R.C. McLean, S.M. George.** 2008, The journal of physical chemistry C, Vol. 112, pp. 4573-4580.

[27] *Metalorganic chemical vapor deposition of aluminum oxide on Si: evidence of interface SiO_2 formation.* **A.R. Chowdhuri, C.G. Takoudis, R.F. Klie, N.D. Browning.** 22, 2002, Applied Physics Letters, Vol. 80, pp. 4241-4243.

[28] *Firing stable Al_2O_3/SiN_x layer stack passivation for the front side boron emitter of n-type silicon solar cells.* **A. Richter, S. Henneck, J. Benick, M. Horteis, M. Hermle, S.W. Glunz.** Valencia, Spain : s.n., September 6-10, 2010, Presented at the 25th European PV Solar Energy Conference and Exhibition .

[29] *Infra-red of inorganic aluminates and characteristic vibration frequencies of AlO_4 and AlO_6.* **P. Tarte.** 7, 1967, Spectrochimica Acta, Vol. 23, pp. 2127-2143.

[30] *Properties of aluminum oxide thin films deposited by pulsed laser deposition and plasma enhanced chemical vapor deposition.* **C. Cibert, H. Hidalgo, C. Champeaux, P. Tristant, C. Tixier, J. Desmaison, A. Catherinot.** 2008, Thin Solid Films, Vol. 516, pp. 1290-1296.

[31] *Plasma and thermal ALD of Al_2O_3 in a commercial 200 mm ALD reactor.* **J.L. van hemmen, S.B.S. Heil, J.H. Klootwijk, F. Roozeboom, C.J Hodson, M.C.M. van de Sanden, W.M.M. Kessels.** 7, 2007, Journal of Electochemical Society , Vol. 154, pp. G165-G169.

[32] *Atomic layer deposition of boron nitride using sequential exposures of BCl_3 and NH_3.* **J.D. Ferguson, A.W. Weimer, S.M. George.** 2002, Thin Solid Films, Vol. 413, pp. 16-25.

[33] *Infrared spectroscopic analysis of the Si/SiO_2 interface structure of thermally oxidized silicon.* **K.T. Queeney, M.K. Weldon, J.P. Chang, Y.J. Chabal, A.B. Gurevich, J. Sapjeta, R.L. Opila.** 3, 2000, Journal of Applied Physics, Vol. 87, pp. 1322-1330.

[34] *Al_2O_3 Atomic layer deposition with trimethylaluminum and ozon studied by in situ transimission FTIR spectroscopy and quadrupole mass spectroscopy.* **D.N. Goldstein, J.A. McCormick, S.M. George.** 2008, Journal of Physical Chemistry, Vol. 112, pp. 19530-19539.

[35] *Plasma-assisted atomic layer deposition of Al_2O_3 at room temperature.* **T.O Kaarianinen, D.C. Cameron.** S1, Plasma Processes and Polymers, Vol. 6, pp. S237-S241.

[36] *The application of diffuse reflectance infrared spectroscopy and temperature-programmed desorption to investigate the interaction of methanol on n-alumina.* **A.R. McInroy, D.T. Lundie, J.M. Winfield, C.C. Dudman, P. Jones, D. Lennon.** 24, 2005, Langmuir, Vol. 21, pp. 11092-11098.

[37] *Impact of annealing-induced compaction on electronic properties of atomic-layer-deposited Al_2O_3.* **V.V. Afanas'ev, A. Stesmans, B.J. Mrstik, C. Zhao.** 9, August 26, 2002, Applied Physics Letters, Vol. 81, pp. 1678-1680.

[38] *Mechanical stress in ALD-Al_2O_3 films.* **G. Krautheim, T. Hecht, S. Jakschik, U. Schroder, W. Zahn.** 2005, Applied Surface Science, Vol. 252, pp. 200-204.

[39] *Directed evolution of a-grains in thin metastable-Al_2O_3 films deposited on Si(100) after post-deposition annealing.* **S.B. Lee, C.W. Ahn, S.-H. Lee, E. K. Her, K.H. Oh, D.-Y. Kim, D.N. Lee.** 2010, Thin Solid Films, Vol. 518, pp. 4304-4311.

[40] *Physical characterization of thin ALD-Al_2O_3 films.* **S. Jakschik, U. Schroeder, T. Hecht, D. Krueger, G. Dollinger, A. Bergmaier, C. Luhmann, J.W. Bartha.** 2003, Applied surface science, Vol. 211, pp. 352-359.

[41] *Thermal stablility and phase transformations of y-/amorphous-Al_2O_3 thin films.* **P. Eklund, M. Sridharan, G. Sing, J. Bottiger.** 2009, Plams Processes and Polymers, Vol. 6, pp. S907-S911.

[42] *Strucutural characterization of phase transition of Al_2O_3 nanopowders obtained by polymeric precursor method.* **S. Cava, S.M. Tebcherani, I.A. Souza, S.A. Pianaro, C.A. Paskocimas, E. Longo, J.A. Varela.** 2007, Materials Chemistry and Physics, Vol. 103, pp. 394-399.

[43] **L.B. Freund, S. Suresh.** *Thin Film Materials; stress. defect formation and surface evolution.* 2003.

[44] *A theoretical and numerical study of a thin clamped circular film under an external load in the presence of a tensile residual stress.* **K.-T. Wan, S. Guo, D.A. Dillard.** 2003, Thin Solid Film, Vol. 425, pp. 150-162.

[45] *Mechanical stress as a function of temperature for aluminum alloy films.* **D.S. Gardner, P.A. Flinn.** 1990, Journal of Applied Physics, Vol. 67, p. 1831.

[46] *On the blistering of atomic layer deposited Al_2O_3 as Si surface passivation.* **B. Vermang, H. Goverde, A. Lorenz, A. Uruena, G. Vereecke, J. Meerschaut, E. Cornagliotti, A. Rothschild, J. John, J. Poortmans, R. Mertens.** Seattle, US : IEEE PVSC, 2011.

[47] *Comprehensive Analytical Model for Locally Contacted Rear Surface Passivated Solar Cells.* **A. Wolf, D. Biro, J. Nekarda, S. Stumpp, A. Kimmerle, S. Mack, R. Preu.** 2010, Journal of Applied Physics, Vol. 105, p. 124510.

[48] *Blistering in ALD Al_2O_3 passsivation layers as rear contacting for local Al BSF Si solar cells.* **B. Vermang, H. Goverde, A. Uruena, A. Lorenz, E. Cornagliotti, A. Rothschild, J. John, J. Poortmans, R. Mertens.** 2012, Solar energy materials and solar cells , Vol. in press.

[49] *Full screen-printed PERC cells with laser-fired contacts - an industrial cell concept with 19.5 % efficiency.* **T. Boscke, R. Hellreigel, T. Wutherich, L. Bornschein, A. Helbig, R. Carl, M. Dupke, D. Stichtenoth, T. Aichele, R. Jesswein, T. Roth, C. Schollhorn, T. Geppert, A. Grohe, J. Lossen. H.-J. Krokoszinski.** Seatlle : 37th IEEE PVSC , 2011. Vol. in press.